

Supersonic and Hypersonic Flows on 2D Unstructured Context: Part II

EDISSON SÁVIO DE GÓES MACIEL

IEA – Aeronautical Engineering Division

ITA – Aeronautical Technological Institute

Praça Mal. Eduardo Gomes, 50 – Vila das Acácias – São José dos Campos – SP – 12228-900

BRAZIL

edissonsavio@yahoo.com.br

Abstract: - In this work, numerical simulations involving supersonic and hypersonic flows on an unstructured context are analyzed. The Van Leer and the Radespiel and Kroll schemes are implemented on a finite volume formulation, using unstructured spatial discretization. The algorithms are implemented in their first and second order spatial accuracies. The second order spatial accuracy is obtained by a linear reconstruction procedure based on the work of Barth and Jespersen. Several non-linear limiters are studied, as well two types of linear interpolation, based on the works of Frink, Parikh and Pirzadeh and of Jacon and Knight. Two types of viscous calculation to the laminar case are compared. They are programmed considering the works of Long, Khan and Sharp and of Jacon and Knight. To the turbulent simulations, the Wilcox and Rubesin model is employed. The ramp problem for the inviscid supersonic simulations and the re-entry capsule for the viscous hypersonic simulations are considered. The results have demonstrated that the Van Leer algorithm yields the best results in terms of the prediction of the wall pressure distribution and the shock angle in the inviscid simulations and the best value of the stagnation pressure at the configuration nose in the viscous simulations. Moreover, the Van Leer algorithm in the SS case and using the Wilcox and Rubesin turbulence model predicts the best value of the lift aerodynamic coefficient. Hence, the Wilcox and Rubesin model yielded good results, proving its good capacity to predict high hypersonic flows. This paper is the second part of this work and is concerned with the laminar and turbulent viscous results.

Key-Words: - Supersonic and hypersonic flows; Unstructured discretization; Van Leer algorithm; Radespiel and Kroll algorithm; Wilcox and Rubesin turbulence model; Euler and Navier-Stokes equations; Two-dimensions.

1 Introduction

Conventional non-upwind algorithms have been used extensively to solve a wide variety of problems [1]. Conventional algorithms are somewhat unreliable in the sense that for every different problem (and sometimes, every different case in the same class of problems) artificial dissipation terms must be specially tuned and judiciously chosen for convergence. Also, complex problems with shocks and steep compression and expansion gradients may defy solution altogether.

Upwind schemes are in general more robust but are also more involved in their derivation and application. Some upwind schemes that have been applied to the Euler equations are, for example, [2], [3] and [4]. For a detailed motivation to study [2] and [4] algorithms, as also their extension to second order of spatial accuracy resulting from a linear reconstruction procedure and the use of a turbulence model to predict turbulence effects, the reader is motivated to read the first part of this work (see [5]).

In this paper, the second of this work, numerical simulations involving hypersonic flows on an unstructured context are analyzed. The [2] and [4] schemes are implemented on a finite volume formulation, using unstructured spatial discretization. The algorithms are implemented in their first order spatial accuracy. Two types of linear interpolation, based on the works of [6] and [7], are studied. Two types of viscous calculation to the laminar case are compared. They are programmed considering the works of [7] and [8]. To the turbulent simulations, the [9] model is employed. The ramp problem to the supersonic inviscid case and the re-entry capsule problem to the hypersonic viscous case are considered. The results have demonstrated that the [2] algorithm yields the best results in terms of the prediction of the wall pressure distribution and the shock angle in the inviscid simulations and the best value of the stagnation pressure at the configuration nose in the viscous simulations. Moreover, the [2] algorithm in the SS case and using the [9] turbulence model predicts the

best value of the lift aerodynamic coefficient. Hence, the [9] model yielded good results, proving its good capacity to predict high hypersonic flows. This paper is the second part of this work and is concerned with the laminar and turbulent results.

2 Results

Two problems were studied in this work, namely: the inviscid supersonic flow along a ramp geometry and the viscous hypersonic flow around a re-entry capsule geometry. The re-entry capsule configuration as also the type of boundary contours are described in Figs. 1 and 2. To the inviscid supersonic flow studied in Part I of this work, the reader is encouraged to read [5]. The Numerical experiments were run on a Notebook computer with dual core processor of 2.13GHz of clock and 4.0 GB of RAM. The criterion adopted to reach the steady state was to consider a reduction of three (3) orders of magnitude in the value of the maximum residual in the calculation domain, a typical CFD community criterion. The maximum residual is defined as the maximum value obtained from the discretized equations in the overall domain, considering all conservation equations. The necessary tables to run the unstructured algorithms are generated in a pre-process stage. The initial conditions to the re-entry capsule problem are described in Tab. 1.

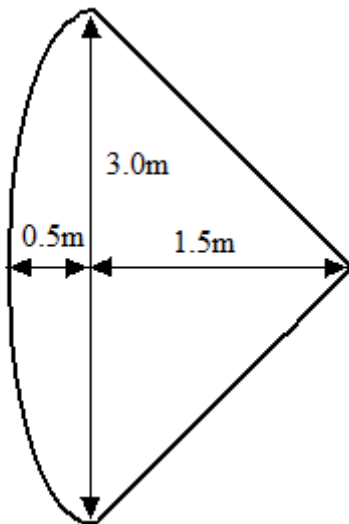


Figure 1: Re-entry Capsule Configuration.

To the viscous cases, the Reynolds number was obtained from data of [10]. To the re-entry capsule problem, considering the freestream Mach number of 10.0, the reference length of 3.0m and an altitude of 40,000m, the Reynolds number is equal to 2.376×10^6 , which characterizes a turbulent flow.

Second order solutions were not obtained by the viscous simulations. Hence, only the first order solutions are presented. Although more diffusive, they gives the general aspect of the solution.

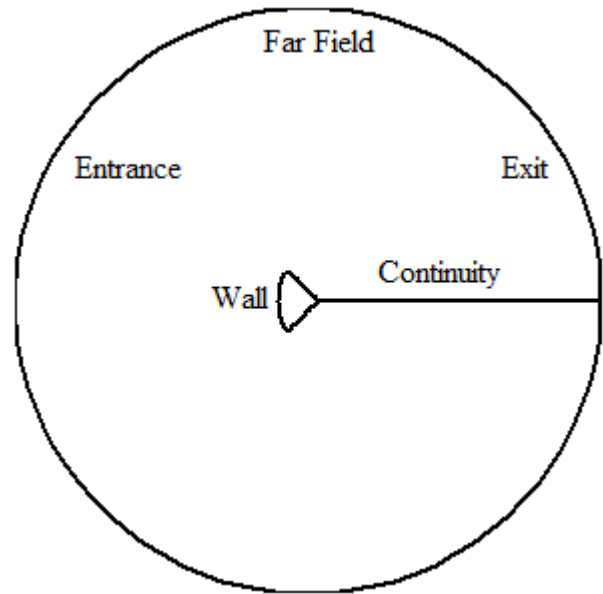


Figure 2: Re-entry Capsule Computational Domain.

Problem:	Property:	Value:
Re-entry Capsule	Freestream Mach, M_∞	10.0
	Angle of Attack, $^\circ$	0.0
	Ratio of specific heats, γ	1.4
	Prd_L	0.72
	Prd_T	0.9
	L_{REF}	3.0m
	Altitude	40,000m

Table 1: Initial Conditions to the Studied Problem.

Problem:	Number of triangular cells:	Number of nodes:
Re-entry Capsule	10,080	5,185

Table 2: Cells and Nodes of the Mesh.

The number of cells and nodes for the re-entry capsule problem are presented in Tab. 2. A mesh of 85x61 nodes, in a finite difference context, is employed.

2.1 First Order Laminar Viscous Solutions – Re-entry Capsule Problem

To this problem were analyzed two types of spatial construction to calculate the viscous gradients. The first one is based on the [8] procedure and the second one is based on [7] procedure.

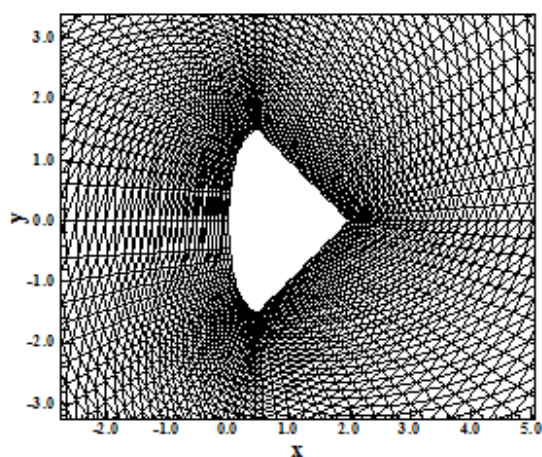


Figure 3: Mesh Oriented in the Same Sense (SS).

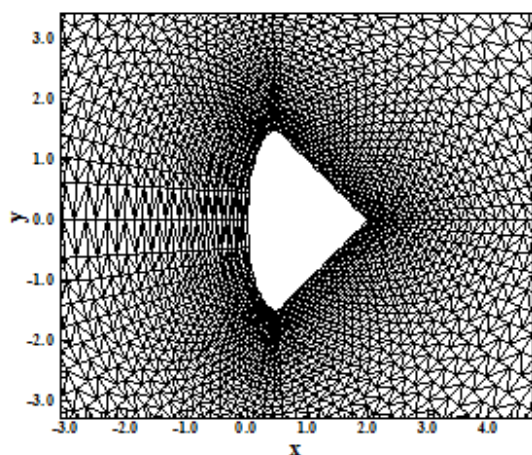


Figure 4: Mesh Oriented in Alternate Sense (AS).

Figures 3 and 4 exhibit the meshes employed in the calculation of the viscous flow to the re-entry calculation. Figure 3 shows the mesh oriented in the same sense (clockwise sense, abbreviated in this paper by “SS”) and Fig. 4 exhibits the mesh oriented in the alternate sense (one row is in clockwise sense and the following is in the counter-clockwise sense, abbreviated in this paper by “AS”). Both cases are analyzed in the laminar case.

2.1.1 Long, Khan and Sharp Procedure

In this procedure, the viscous gradients are calculated by arithmetical average between the left and the right states of the flux interface. Components of the velocity vector are also calculated by arithmetical average. This procedure considers three models of viscosity, as mentioned in [5], namely: constant viscosity (equal to the freestream viscosity), Sutherland formula and [11] model. The results are presented in the aforementioned order.

Case $\mu = \text{Constant}$. In this case, μ was adopted as equal to its freestream value, without variation during the simulation process. Figures 5 to 8 show the pressure field obtained by [2] and [4] in the cases SS and AS. As observed, the most severe pressure field is generated by the [2] scheme in the SS case. Both [2] and [4] solutions present similar symmetry properties. The normal shock wave ahead of the configuration is well characterized in all solutions.

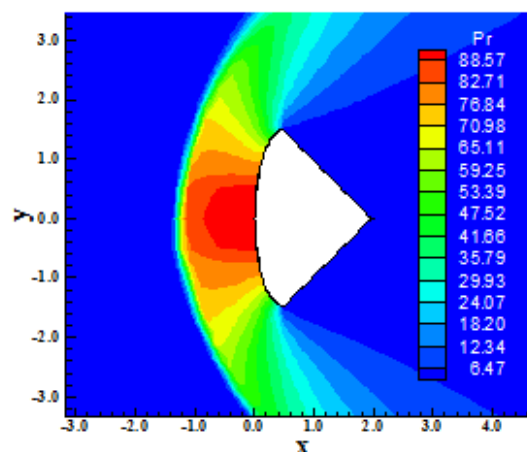


Figure 5: Pressure Field ([2] – SS).

Figures 9 to 12 exhibit the Mach number field obtained by [2] and [4] in cases SS and AS. The most intense Mach number field is due to [4] in the SS case. All solutions present good symmetry characteristics. This is observed more clearly in Figs. 13 to 16. In this viscous problem, the boundary layer suffers a detachment from the configuration walls close to the trailing edge, where the viscous contribution is more meaningful. So, a pair of vortex is formed in this region and is positioned symmetrically in relation to the wake line. Hence, the expected behavior of this pair of vortex is one vortex positioned at the upper surface and the other vortex positioned at the lower surface.

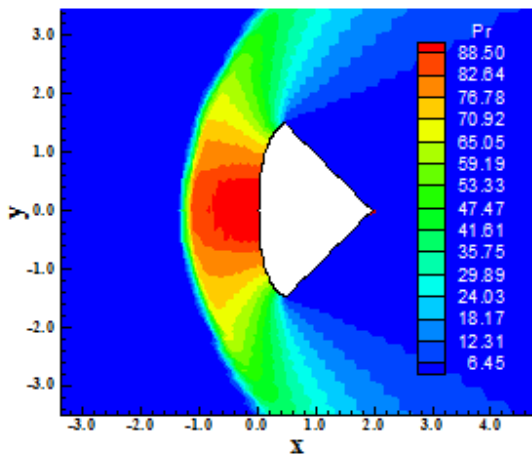


Figure 6: Pressure Field ([2] – AS).

the boundary layer. Figure 18 exhibits the $-C_p$ distribution where practically all solutions converge to the same behavior.

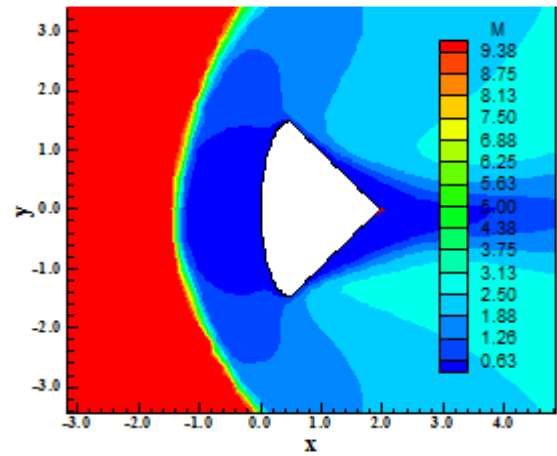


Figure 9: Mach Number Field ([2] – SS).

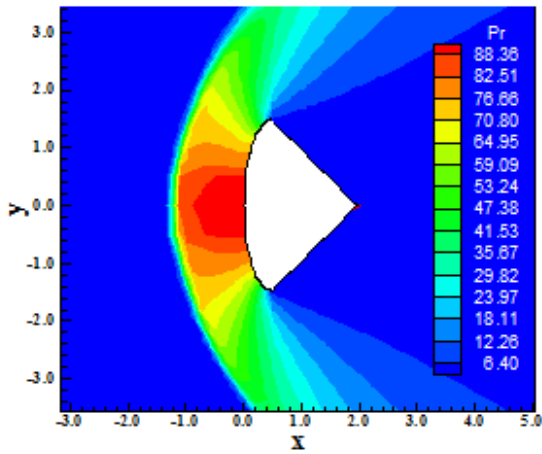


Figure 7: Pressure Field ([4] – SS).

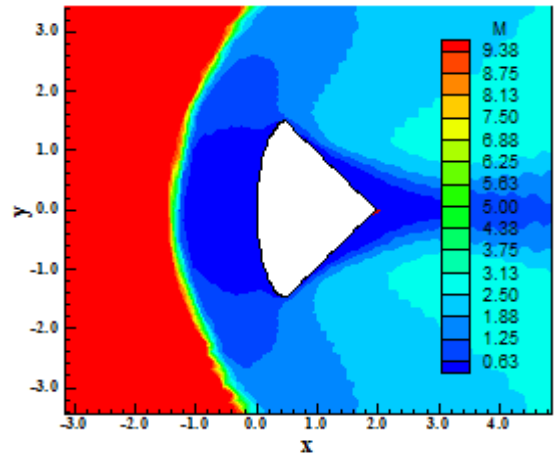


Figure 10: Mach Number Field ([2] – AS).

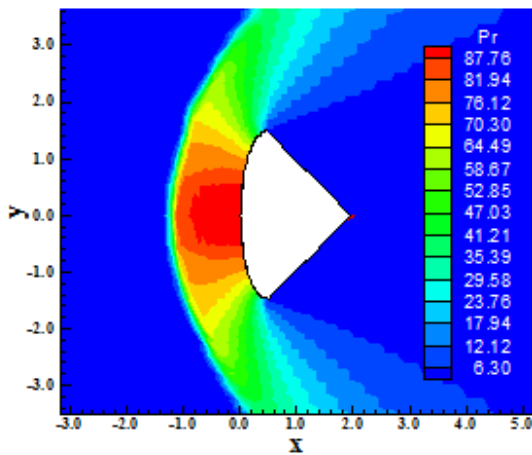


Figure 8: Pressure Field ([4] – AS).

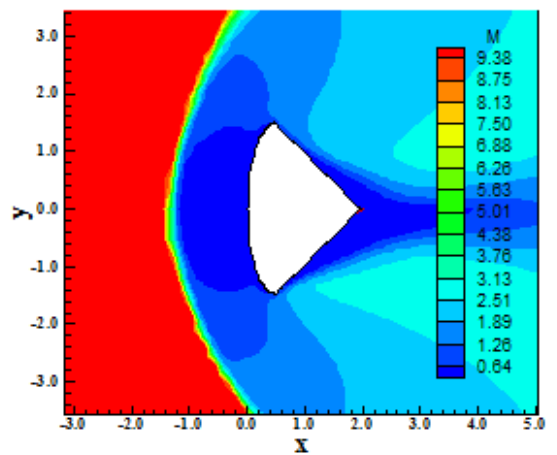


Figure 11: Mach number field ([4] – SS).

Observing Figures 13 to 16, it is clear that the AS cases are the most correct solutions.

Figure 17 shows the C_f distribution around the re-entry capsule wall. Curves of C_f crossing the x-axis define detachment and reattachment points of

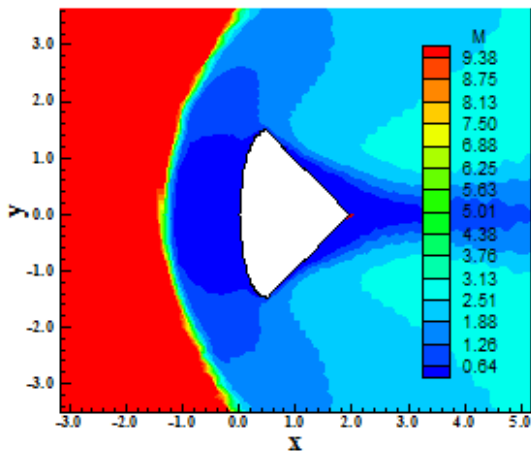


Figure 12: Mach Number Field ([4] – AS).

properties. The most severe pressure field is due to [2] in the SS case. There are not meaningful differences between these solutions and their contra part with the constant μ model.

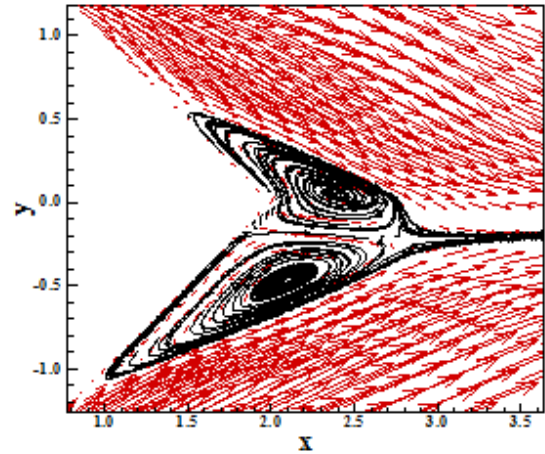


Figure 15: Velocity Field and Streamlines ([4] – SS).

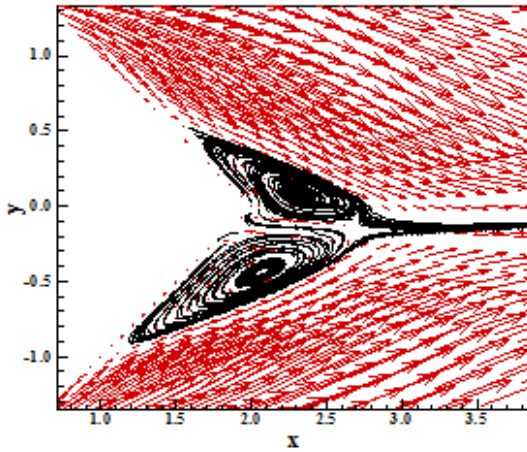


Figure 13: Velocity Field and Streamlines ([2] – SS).

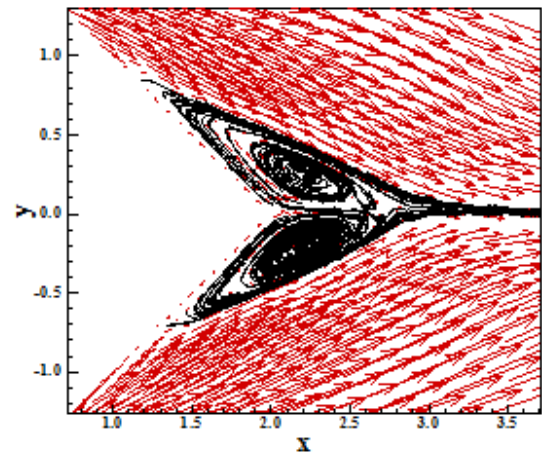


Figure 16: Velocity Field and Streamlines ([4] – AS).

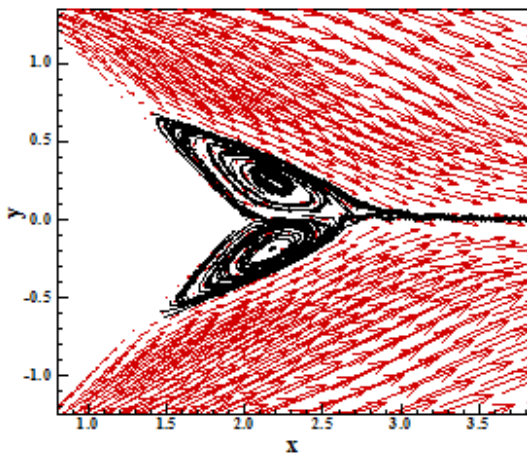


Figure 14: Velocity Field and Streamlines ([2] – AS).

Case μ defined according to Sutherland formula.

In this case, the empirical Sutherland law is applied to obtain the molecular viscosity behavior. Figures 19 to 22 show the pressure field obtained by [2] and [4] in the SS and AS cases as using the Sutherland formula. All solutions present good symmetry

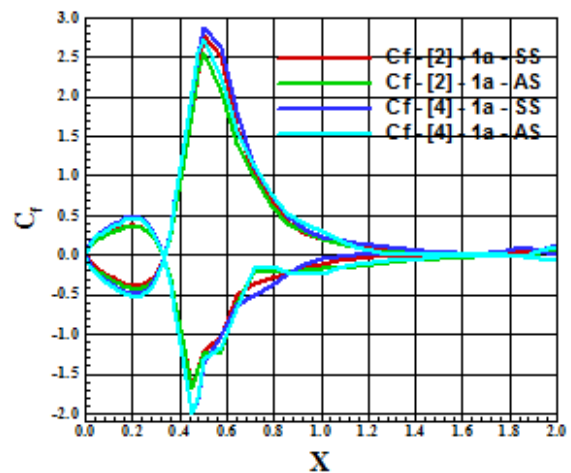


Figure 17: C_f Distribution at Wall.

Figures 23 to 26 exhibit the Mach number field generated by the [2] and [4] algorithms in the SS and AS cases. The Mach number solutions are very similar.

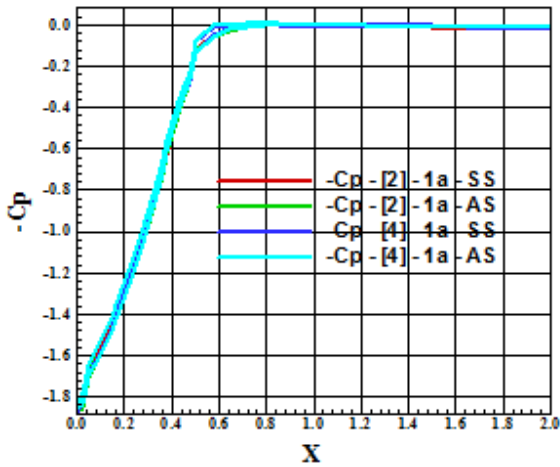


Figure 18: $-C_p$ Distribution at Wall.

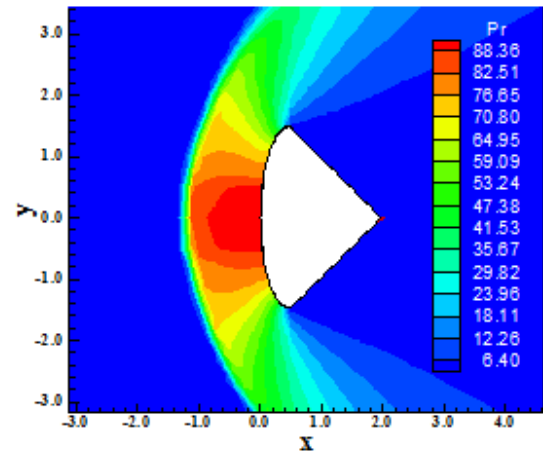


Figure 21: Pressure Field ([4] – SS).

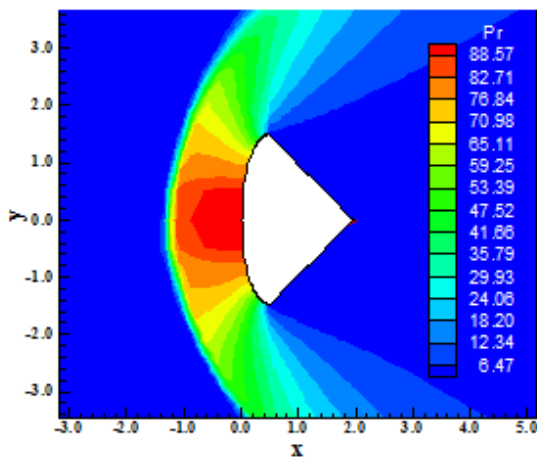


Figure 19: Pressure Field ([2] – SS).

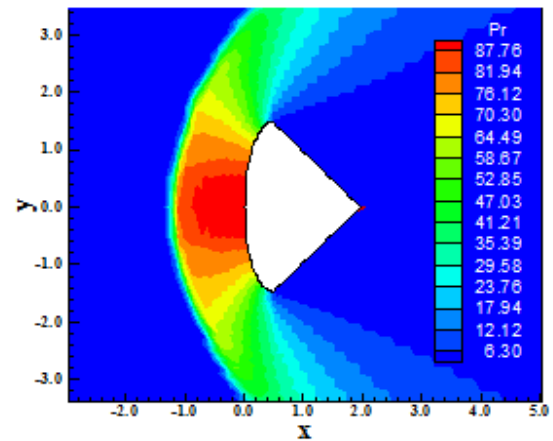


Figure 22: Pressure Field ([4] – AS).

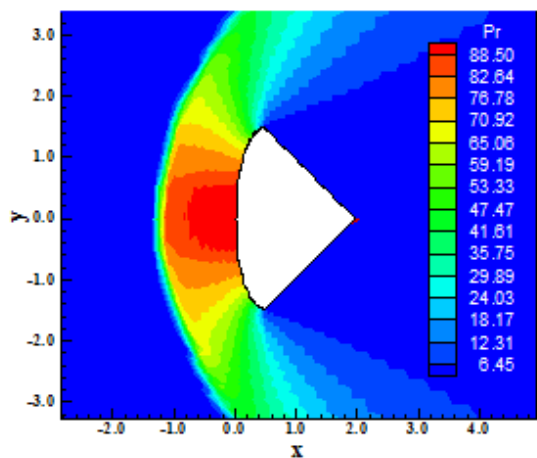


Figure 20: Pressure Field ([2] – AS).

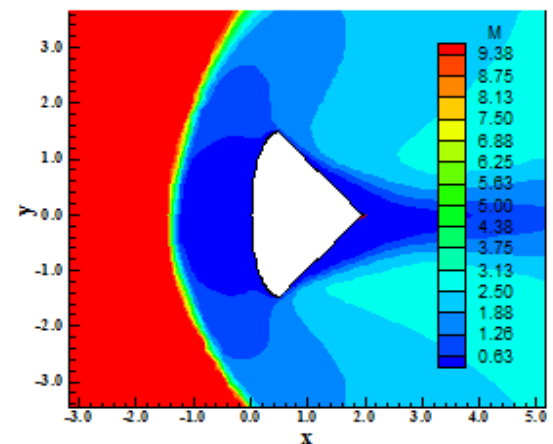


Figure 23: Mach Number Field ([2] – SS).

The most intense Mach number field is obtained with the [4] scheme in both cases SS and AS. All these solutions present good symmetry characteristics, with better behavior to the AS cases at the trailing edge.

Figures 27 to 30 show the vortex field close to the trailing edge of the re-entry capsule. As observed, the SS cases present non-symmetrical characteristics, whereas the AS cases repair these effects and put the pair of vortex in the correct positions.

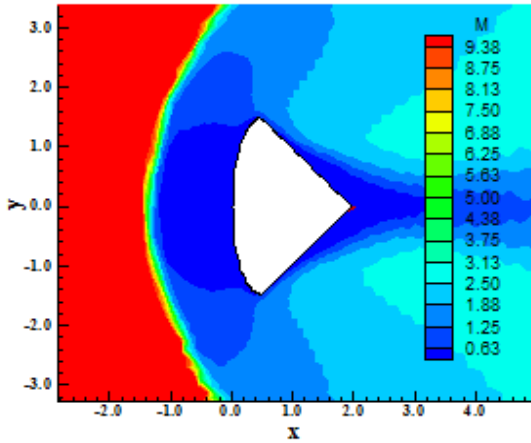


Figure 24: Mach Number Field ([2] – AS).

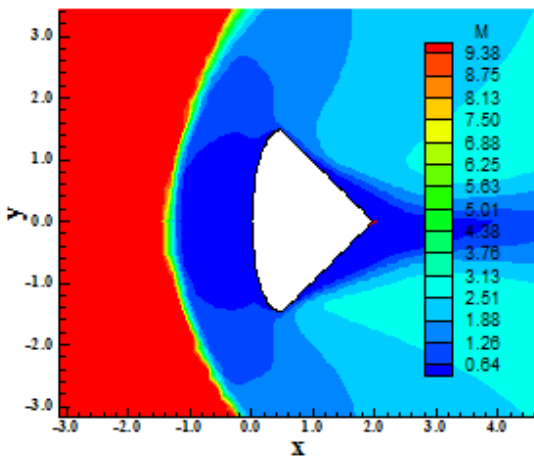


Figure 25: Mach Number Field ([4] – SS).

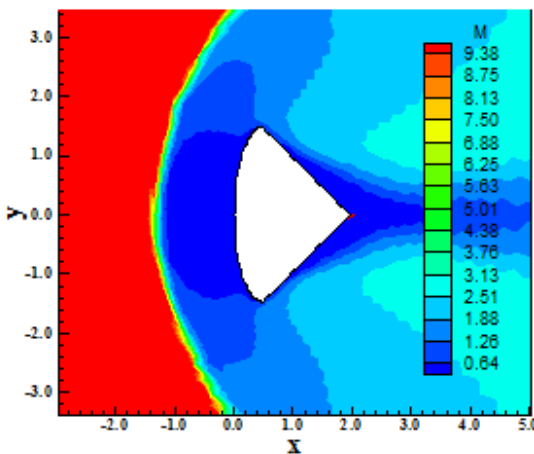


Figure 26: Mach Number Field ([4] – AS).

Figure 31 exhibits the C_f distribution around the re-entry capsule wall. Again, points where the curves of C_f cross the x-axis represent points of detachment and reattachment. Figure 32 shows the $-C_p$ distribution. All curves present similar behavior. The “cut out” effect is observed in the curves of AS solutions, whereas the curves of SS solutions are smooth.

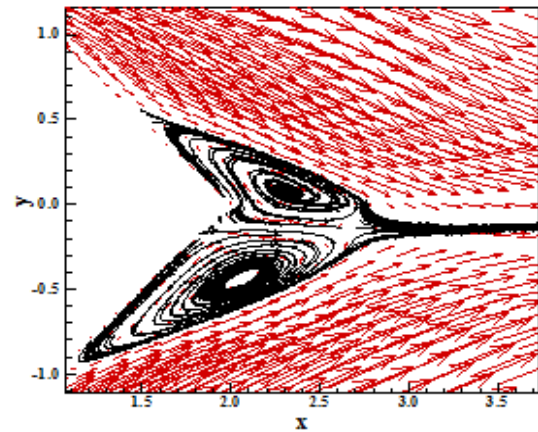


Figure 27: Velocity Field and Streamlines ([2] – SS).

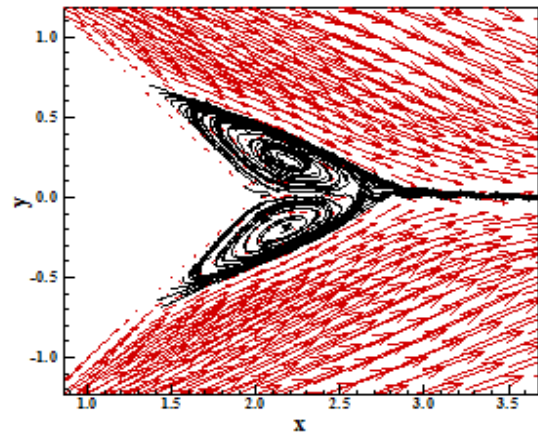


Figure 28: Velocity Field and Streamlines ([2] – AS).

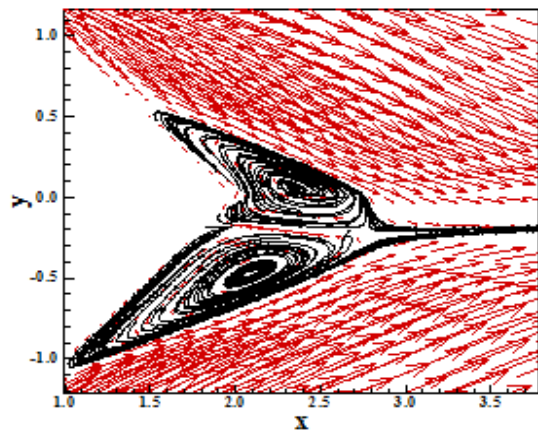


Figure 29: Velocity Field and Streamlines ([4] – SS).

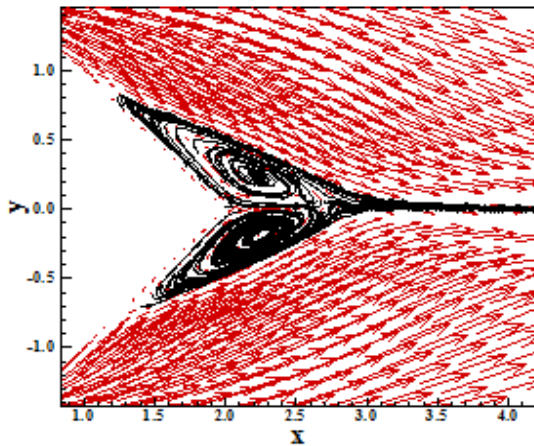


Figure 30: Velocity Field and Streamlines ([4] – AS).

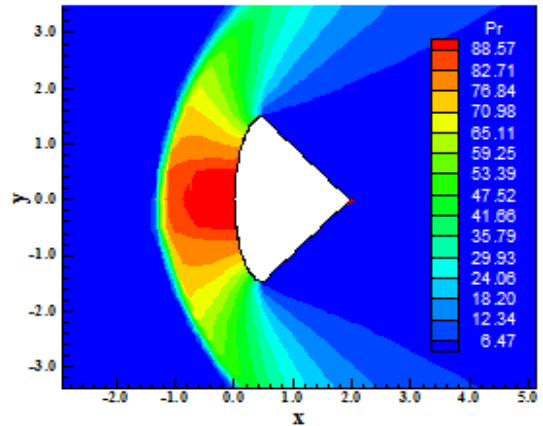


Figure 33: Pressure Field ([2] – SS).

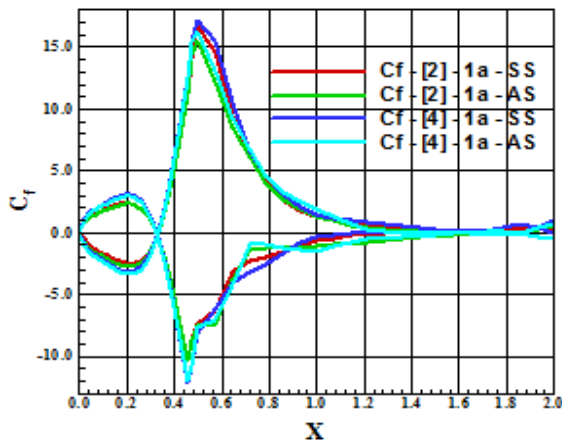


Figure 31: C_f Distribution at Wall.

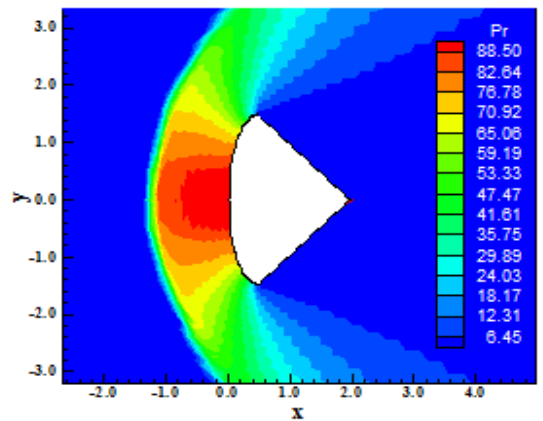


Figure 34: Pressure Field ([2] – AS).

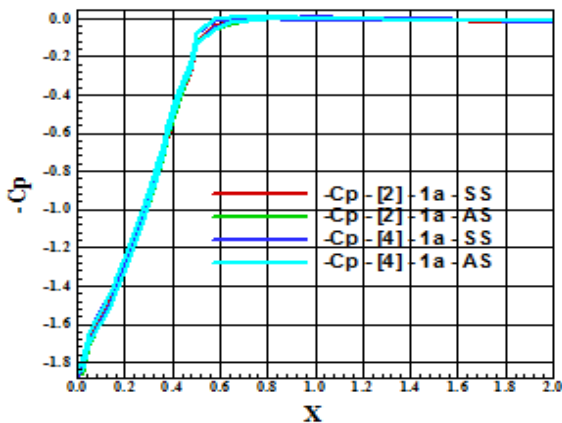


Figure 32: $-C_p$ Distribution at Wall.

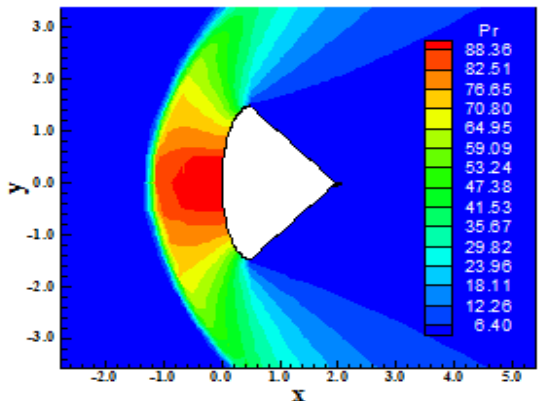


Figure 35: Pressure Field ([4] – SS).

Case μ defined according to [11]. In this case, the model of [11] is applied. This model is simpler than the Sutherland formula, but good solutions are expected. Figures 33 to 36 present the pressure field obtained by the [2] and [4] algorithms in the SS and AS cases. The most severe pressure field is due to [2] in the SS case. None of them are different from the other solutions of μ proposed models. Good

symmetry properties are mainly observed in the [4] solutions.

Figures 37 to 40 show the Mach number field generated by the [2] and [4] schemes in the SS and AS cases. Good symmetry properties are observed in all figures. The most intense Mach number field is generated by the [4] algorithm in both SS and AS cases. Figures 41 to 44 present the vortex field close to the trailing edge of the re-entry capsule. As can

be seen, the SS solutions are non-symmetrical in relation to the x-axis, whereas the AS solutions are symmetrical in relation to this axis.

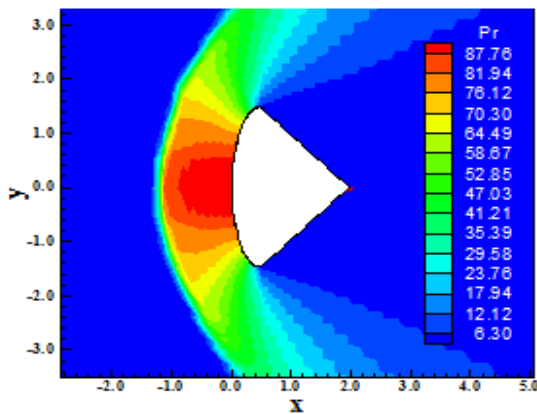


Figure 36: Pressure Field ([4] – AS).

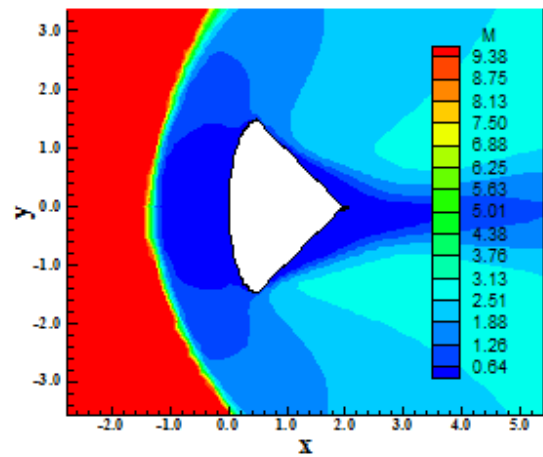


Figure 39: Mach Number Field ([4] – SS).

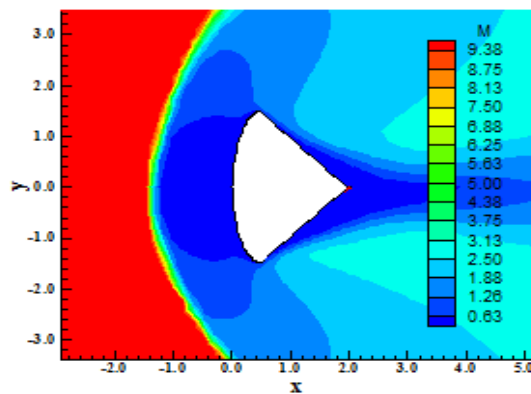


Figure 37: Mach Number Field ([2] – SS).

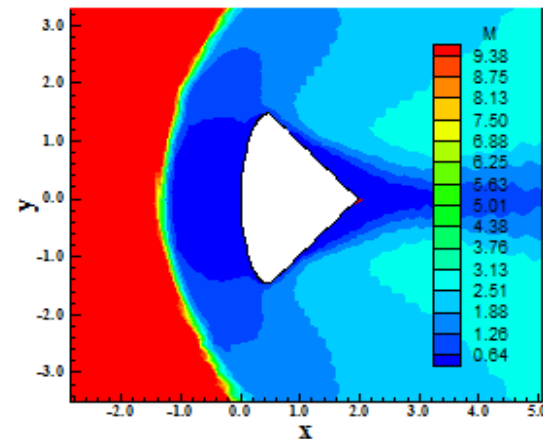


Figure 40: Mach Number Field ([4] – AS).

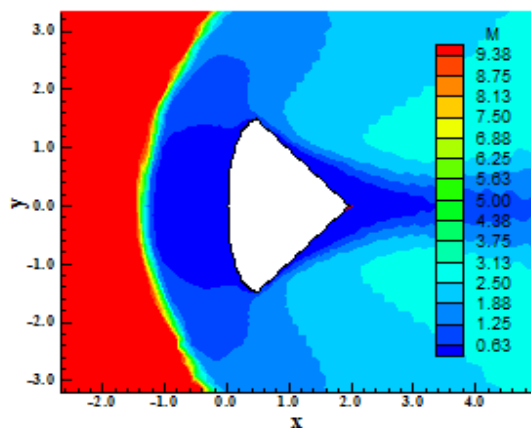


Figure 38: Mach Number Field ([2] – AS).

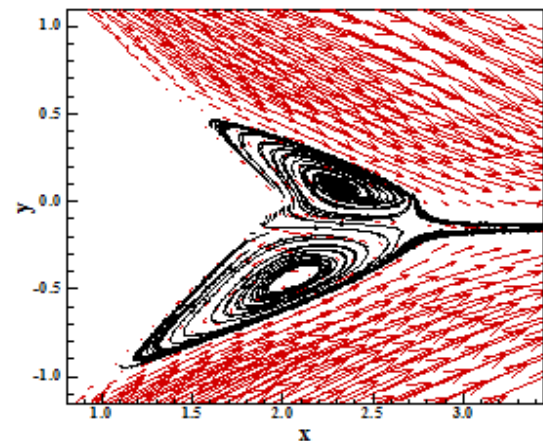


Figure 41: Velocity Field and Streamlines ([2] – SS).

Figure 45 shows the C_f distribution around the re-entry capsule wall. Points of detachment and reattachment are observed. Figure 46 exhibits the $-C_p$ distribution around the re-entry capsule wall. All solutions are similar, without a meaningful difference. The upper and lower pressure surfaces are basically symmetrical.

2.1.2 Jacon and Knight Procedure

In this procedure, the viscous gradients are calculated by the quadrilateral or triangle (boundary cells) of integration. The viscous calculation considers two options of interpolation to obtain the vector of conserved variables at nodes.

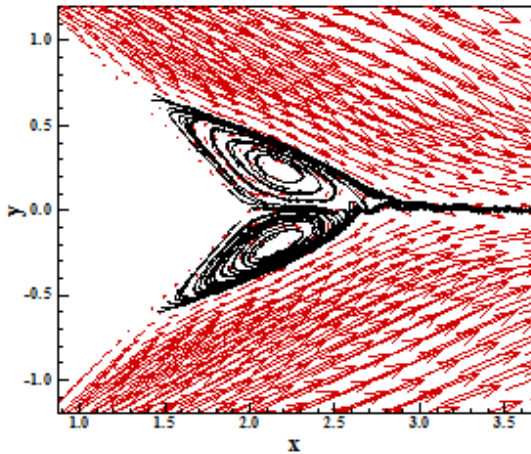


Figure 42: Velocity Field and Streamlines ([2] – AS).

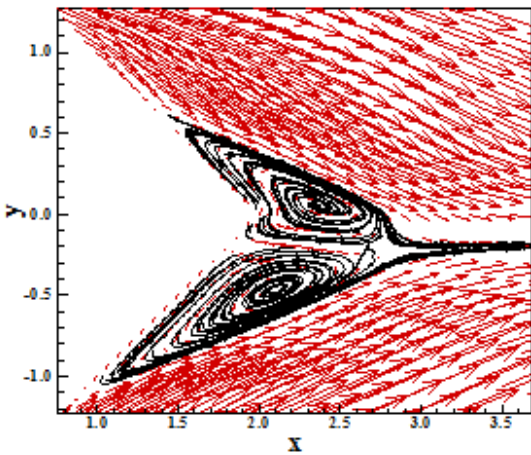


Figure 43: Velocity Field and Streamlines ([4] – SS).

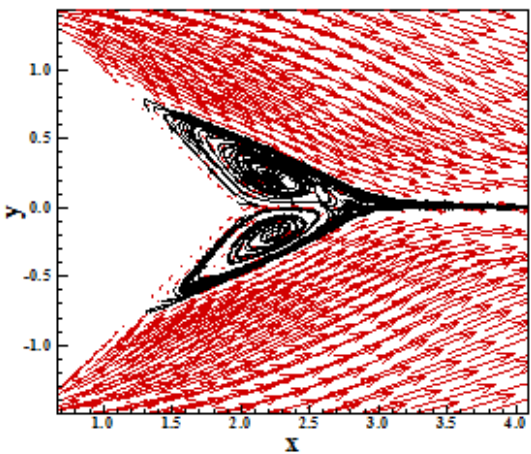


Figure 44: Velocity Field and Streamlines ([4] – AS).

The first one is based in [6] methodology and the second one is based on [7] methodology. Both methodologies consider three models of viscosity, as mentioned in [5], namely: constant viscosity (equal to the freestream viscosity), Sutherland

formula and [11] model. The results are presented in the aforementioned order.

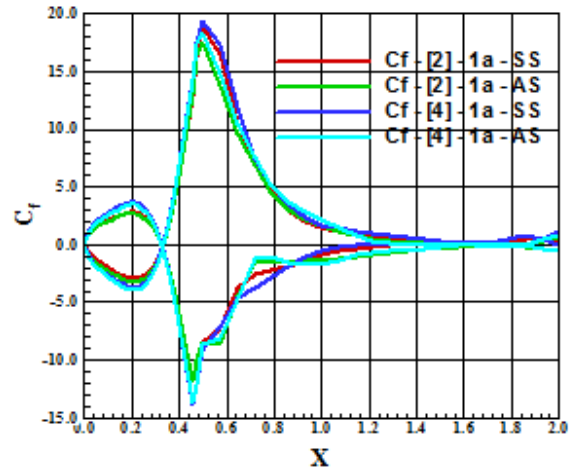


Figure 45: C_f Distribution at Wall.

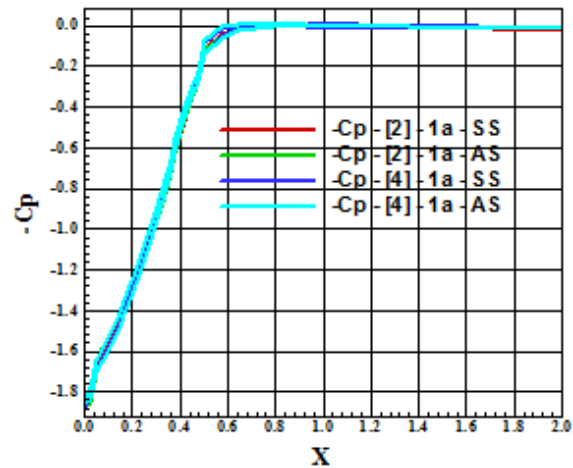


Figure 46: $-C_p$ Distribution at Wall.

Frink, Parikh and Pirzadeh Interpolation. This type of interpolation is described in [5].

Case $\mu = Constant$. Figures 47 to 50 show the pressure field obtained by the [2] and [4] algorithms in the SS and AS cases. Good symmetry properties are observed in all solutions. The most severe pressure field is due to [2] in the SS case.

Figures 51 to 54 exhibit the Mach number field obtained by the [2] and [4] schemes in the SS and AS cases. Good symmetry properties are observed in all solutions. The most intense Mach number field is due to [4] in the SS case.

Figures 55 to 58 show the vortex field obtained by the [2] and [4] algorithms in the SS and AS cases. As can be seen, the SS cases present a non-symmetrical behavior, with a vortex occupying part of the region of the other vortex. On the other hand, the AS cases originate a pair of vortex located at the

actual position, according to the physics of the fluid mechanics.

shows the $-C_p$ distribution at the re-entry capsule wall. All solutions generated by the [2] and [4] schemes in the SS and AS cases are very similar.

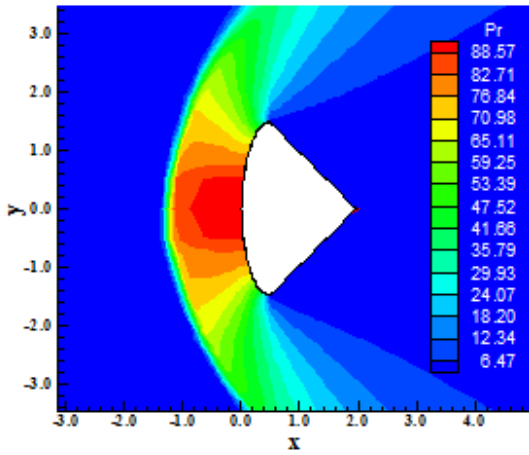


Figure 47: Pressure Field ([2] – SS).

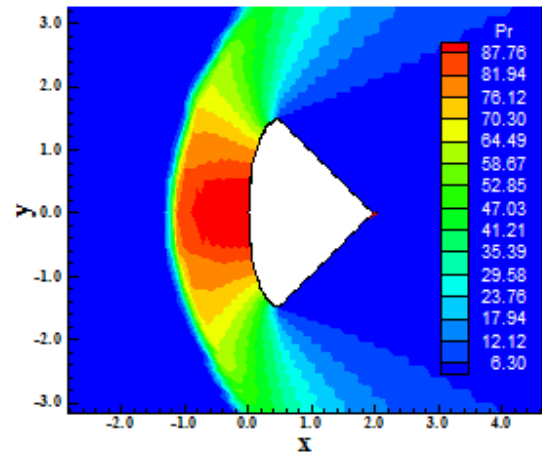


Figure 50: Pressure Field ([4] – AS).

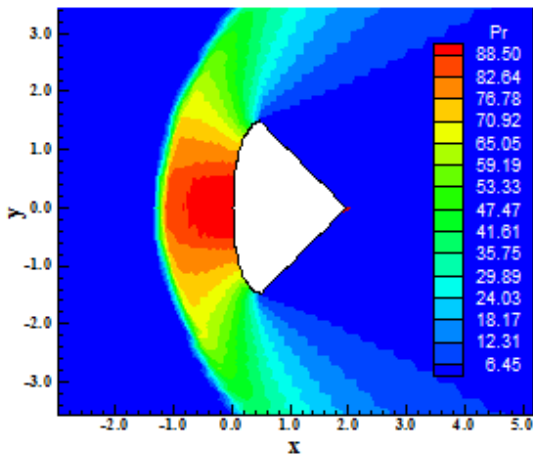


Figure 48: Pressure Field ([2] – AS).

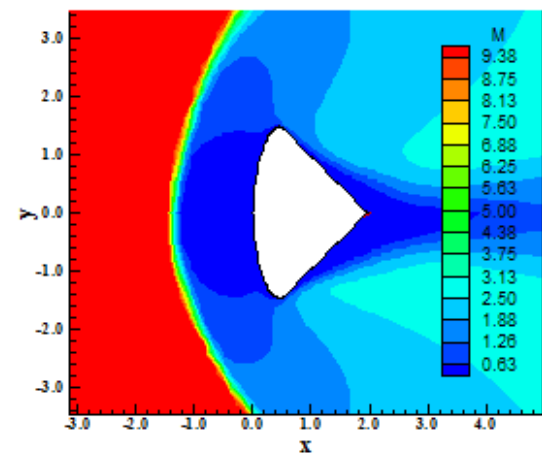


Figure 51: Mach Number Field ([2] – SS).

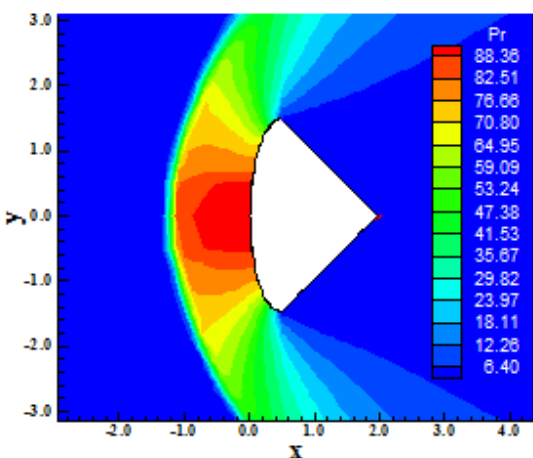


Figure 49: Pressure Field ([4] – SS).

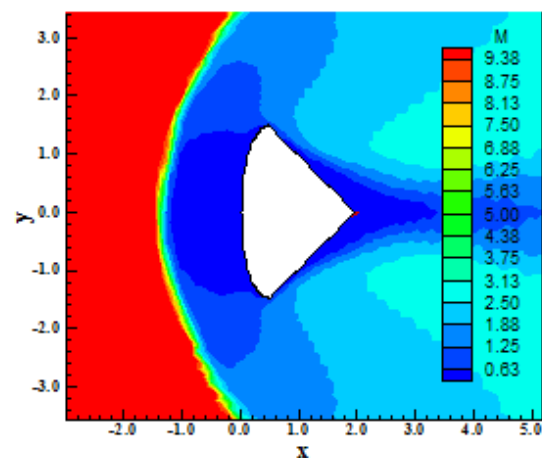


Figure 52: Mach Number Field ([2] – AS).

Figure 59 presents the C_f distribution around the re-entry capsule wall. As can be seen, detachment and reattachment points are perceptible. Figure 60

Case μ defined according to Sutherland formula. Figures 61 to 64 present the pressure field

obtained by the [2] and [4] numerical algorithms in the cases SS and AS. The most severe pressure field is obtained by the [2] algorithm in the SS case. Good symmetry properties are observed, even in the AS case.

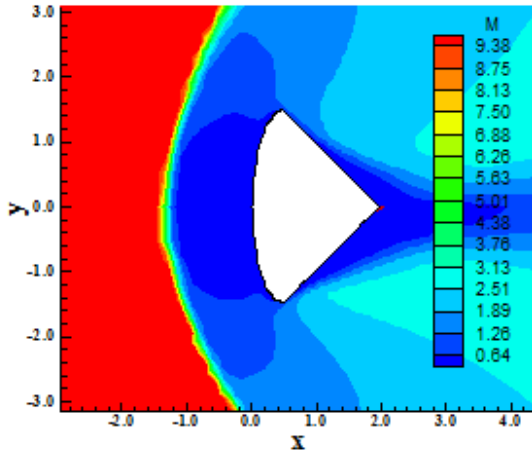


Figure 53: Mach Number Field ([4] - SS).

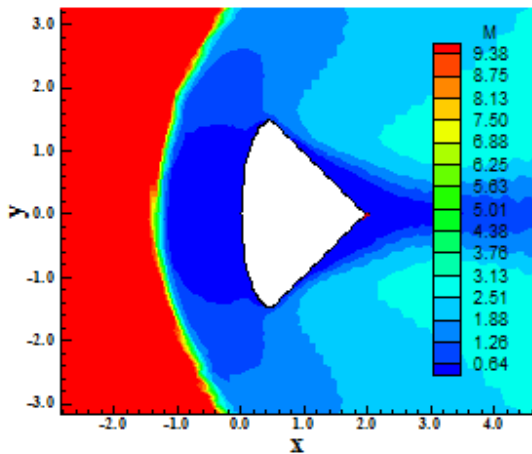


Figure 54. Mach Number Field ([4] - AS).

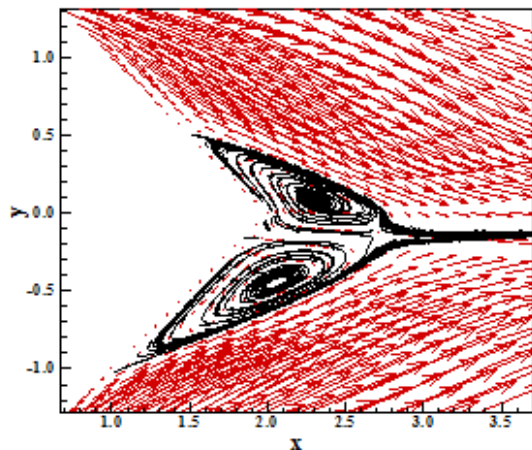


Figure 55: Velocity Field and Streamlines ([2] - SS).

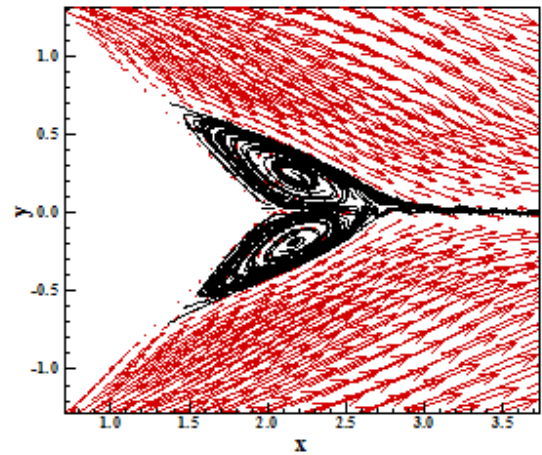


Figure 56: Velocity Field and Streamlines ([2] - AS).

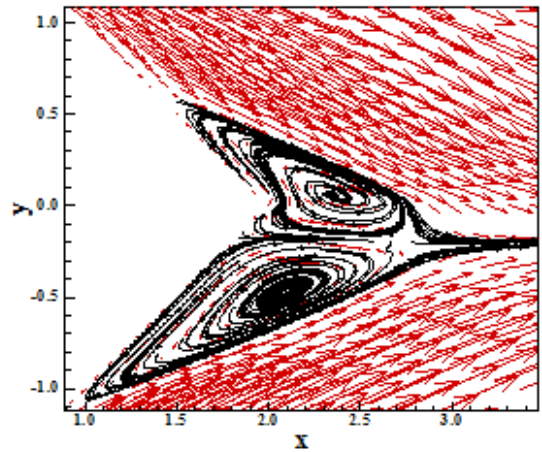


Figure 57: Velocity Field and Streamlines ([4] - SS).

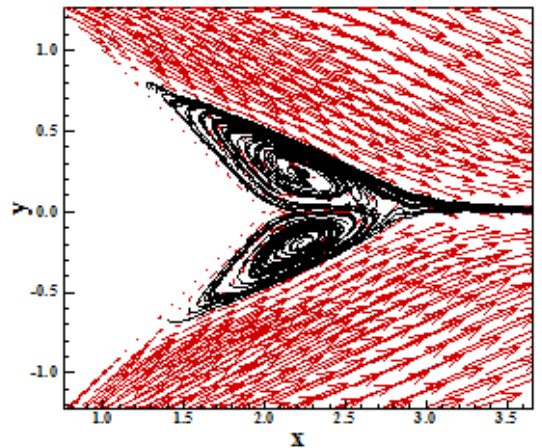


Figure 58: Velocity Field and Streamlines ([4] - AS).

Figures 65 to 68 exhibit the Mach number field obtained by the numerical schemes [2] and [4] in the SS and AS cases. Good symmetry properties are observed and the most intense Mach number field is due to the [4] algorithm in both SS and AS cases.

Figures 69 to 72 show the vortex field captured by the [2] and [4] numerical schemes in the SS and AS cases. As observed in the other studies, the SS solutions present a non-symmetrical field, whereas the AS solutions repair this effect and yield a symmetrical vortex field.

at approximately 0.32m, whereas reattachment points are located at approximately 1.60m. Figure 74 presents the $-C_p$ distributions at the re-entry capsule wall. All solutions converge to a similar behavior.

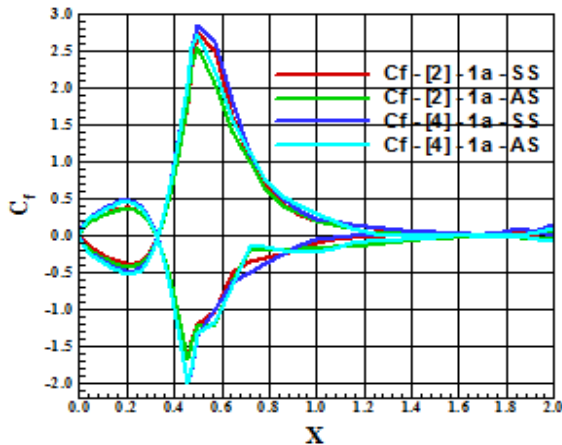


Figure 59. C_f Distribution at Wall.

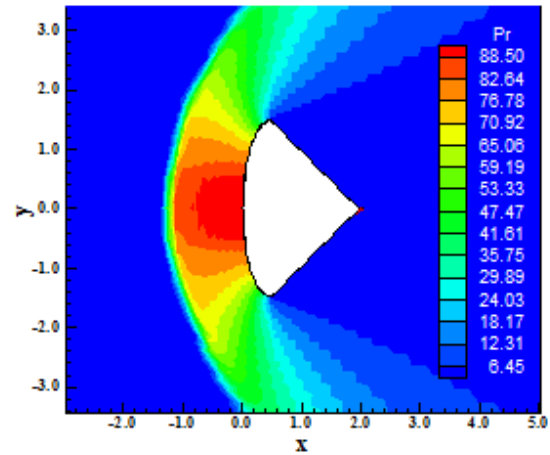


Figure 62: Pressure Field ([2] - AS).

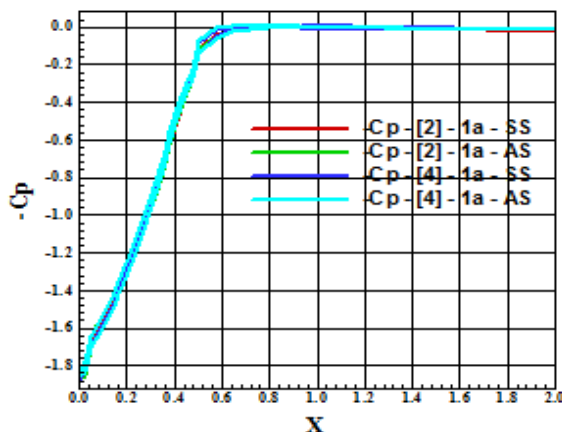


Figure 60. $-C_p$ Distribution at Wall.

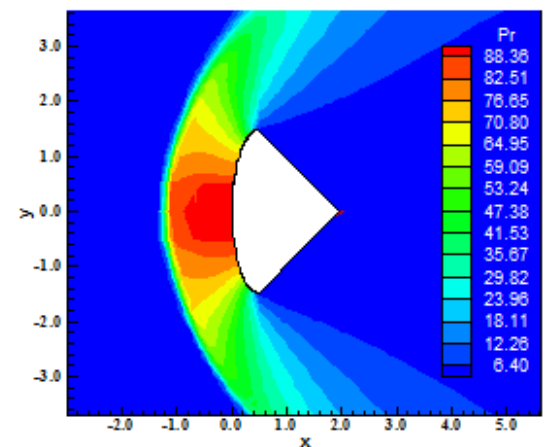


Figure 63: Pressure Field ([4] - SS).

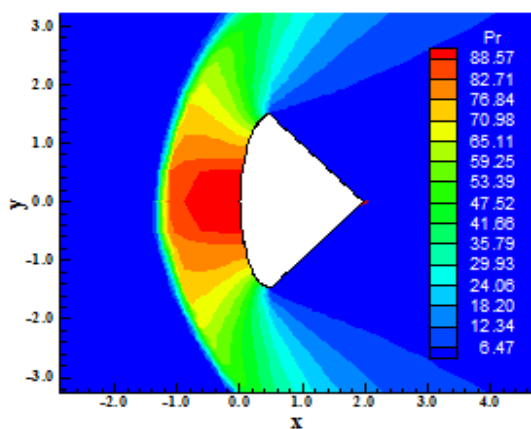


Figure 61: Pressure Field ([2] - SS).

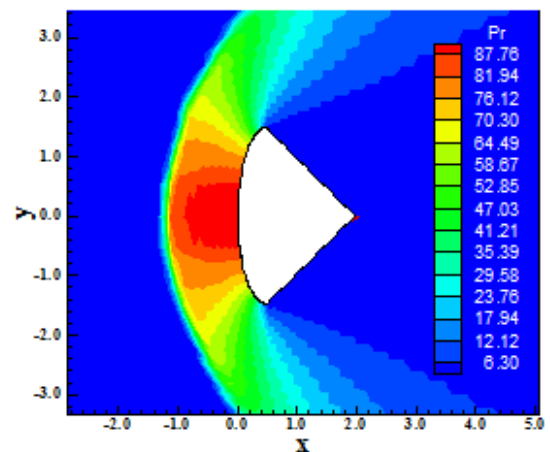


Figure 64: Pressure Field ([4] - AS).

Figure 73 shows the C_f distribution at the re-entry capsule wall. Points of detachment are located

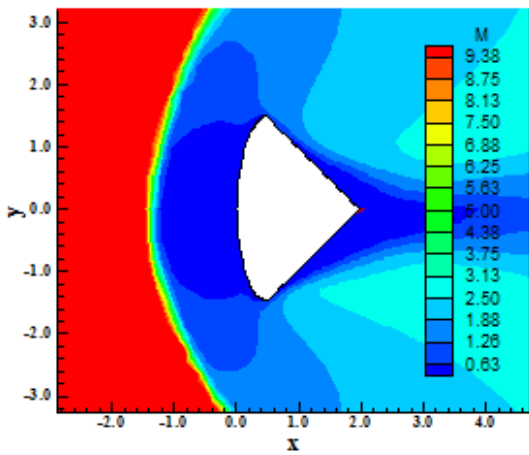


Figure 65: Mach Number Field ([2] – SS).

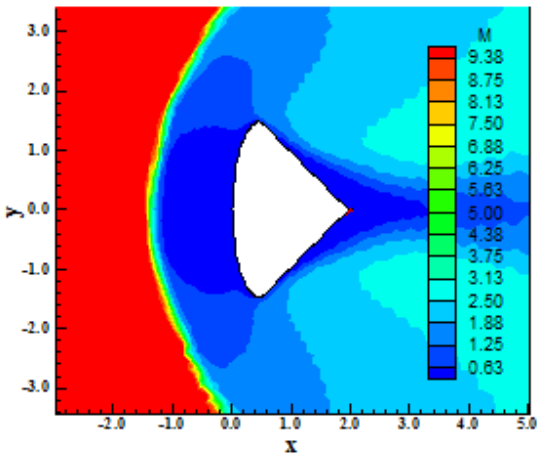


Figure 66: Mach Number Field ([2] – AS).

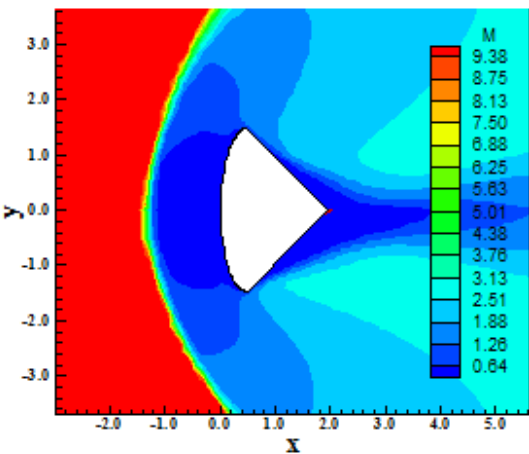


Figure 67: Mach Number Field ([4] – SS).

Case μ defined according to [11]. Figures 75 to 78 present the pressure field obtained by the [2] and [4] schemes in the SS and AS cases. The most severe pressure field is obtained by the [2] scheme in the SS case.

Figures 79 to 82 show the Mach number field generated by the [2] and [4] algorithms in the SS and AS cases. Good symmetry properties are observed. The most intense Mach number field is obtained by the [4] algorithm in both SS and AS cases.

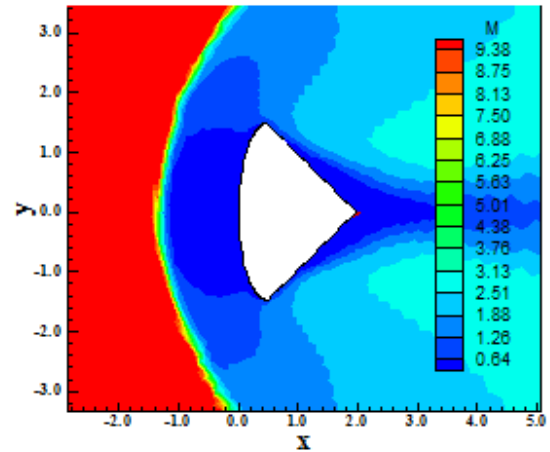


Figure 68: Mach Number Field ([4] – AS).

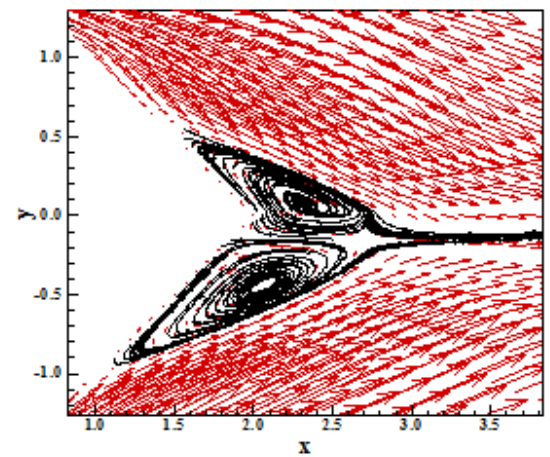


Figure 69: Velocity Field and Streamlines ([2] – SS).

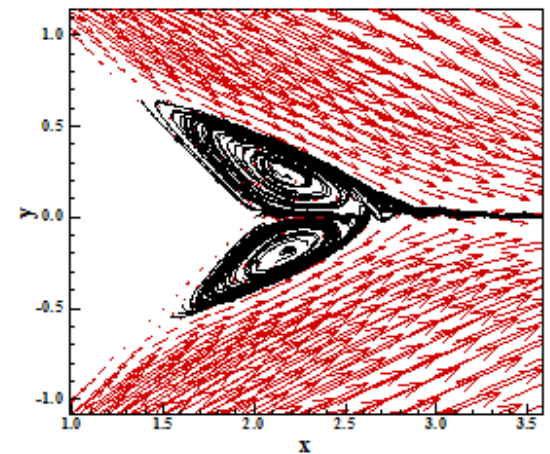


Figure 70: Velocity Field and Streamlines ([2] – AS).

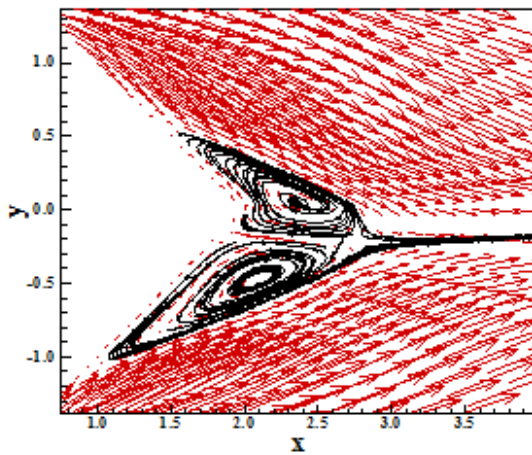


Figure 71: Velocity Field and Streamlines ([4] – SS).

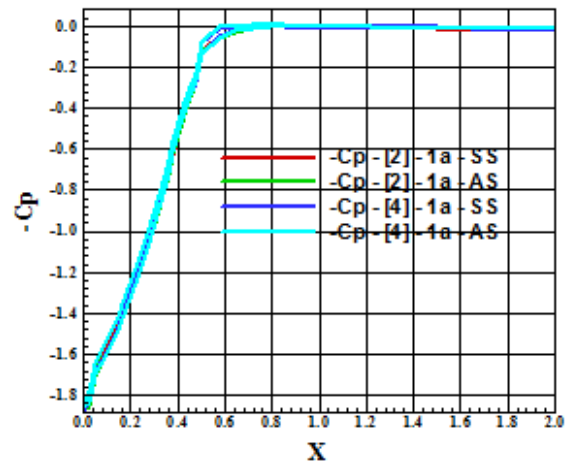


Figure 74. $-C_p$ Distribution at Wall.

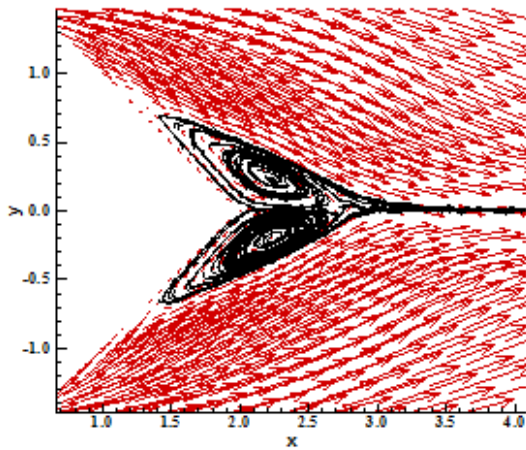


Figure 72: Velocity Field and Streamlines ([4] – AS).

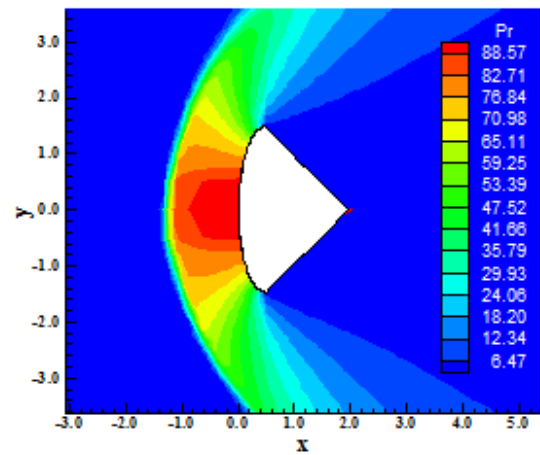


Figure 75: Pressure Field ([2] – SS).

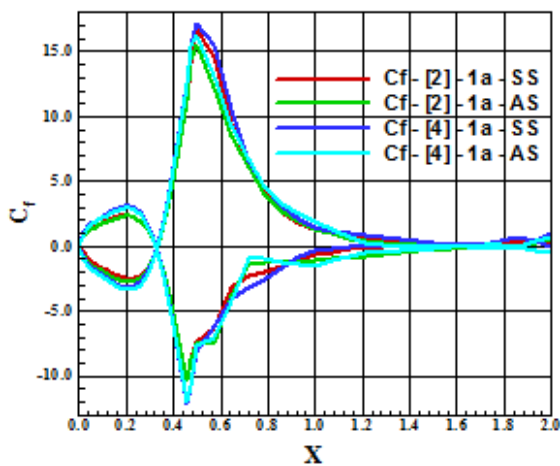


Figure 73. C_f Distribution at Wall.

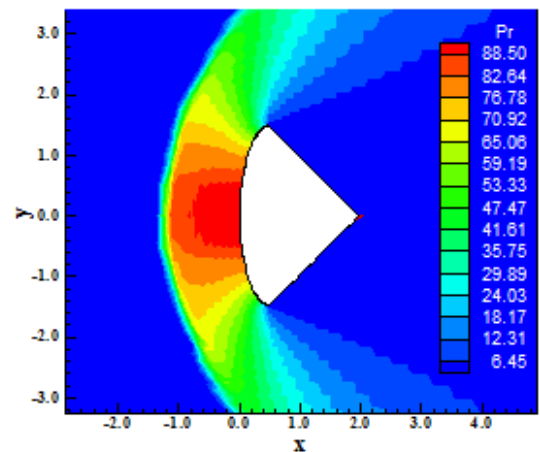


Figure 76: Pressure Field ([2] – AS).

Figures 83 to 86 exhibit the vortex field generated by the [2] and [4] schemes in the SS and AS cases. It is possible to note again the non-symmetrical field in the SS cases and the more symmetrical field in the AS cases.

Figure 87 shows the C_f distribution around the re-entry capsule wall. Detachment and reattachment points are found approximately in 0.32m and 1.60m, respectively. Figure 88 presents the $-C_p$ distribution

at the re-entry capsule wall. The agreement among the curves is blatant.

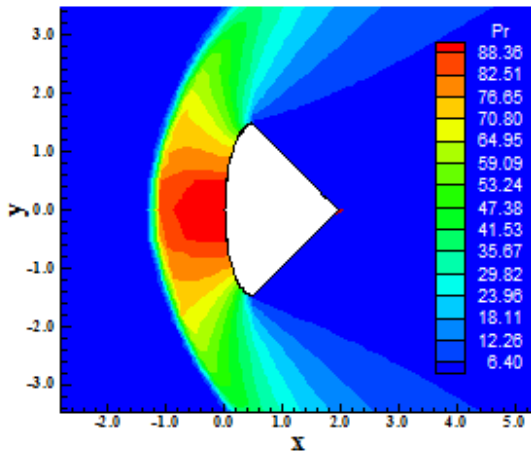


Figure 77: Pressure Field ([4] – SS).

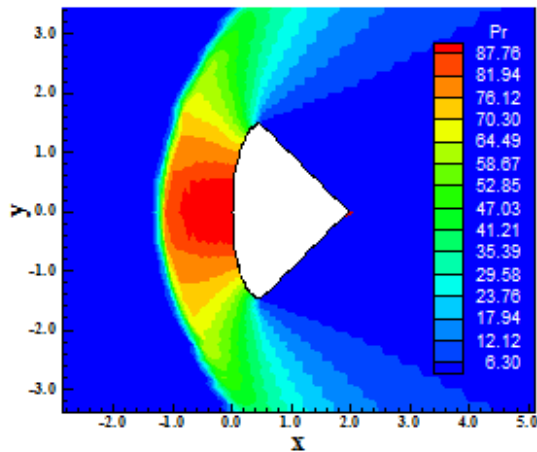


Figure 78: Pressure Field ([4] – AS).

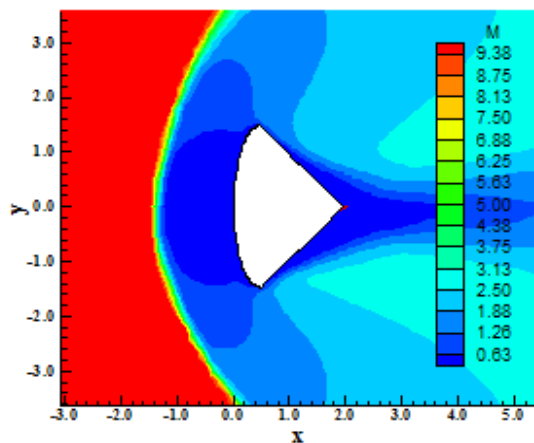


Figure 79: Mach Number Field ([2] – SS).

Jacon and Knight Interpolation. This type of interpolation is described in [5].

Case $\mu = Constant$. Figures 89 to 92 exhibit the pressure field obtained by [2] and [4] in the SS and AS cases. Good symmetry properties are observed in all solutions. The most severe pressure field is due to [2] algorithm in the SS case. The “cut out” effect is again observed.

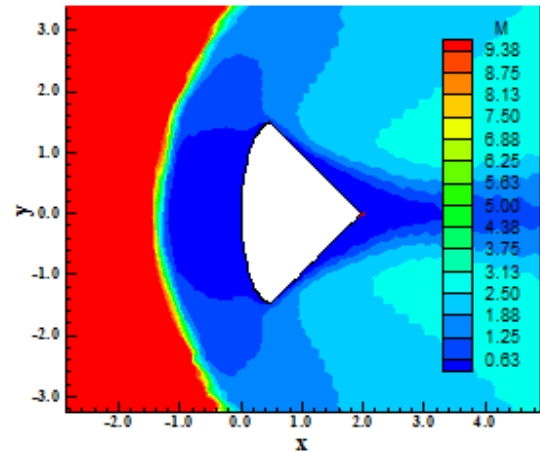


Figure 80: Mach Number Field ([2] – AS).

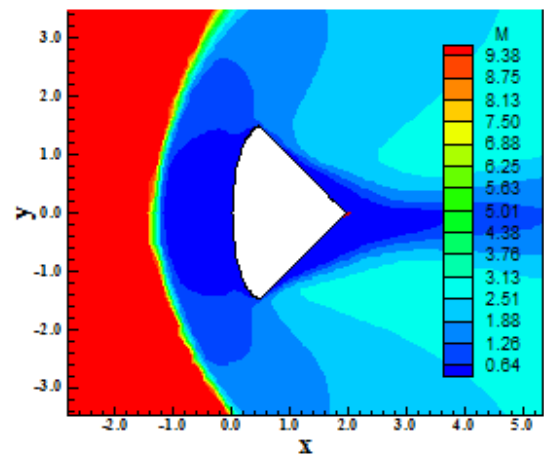


Figure 81: Mach Number Field ([4] – SS).

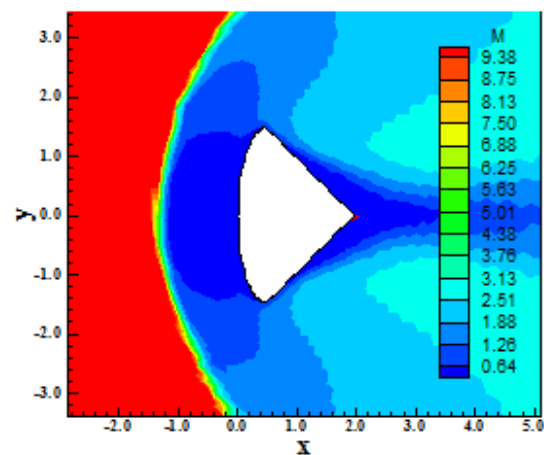


Figure 82: Mach Number Field ([4] – AS).

Figures 93 to 96 show the Mach number field obtained by the [2] and [4] algorithms in the SS and AS cases. The most intense Mach number field is due to [4] in the SS case. Good symmetry properties are observed in all solutions.

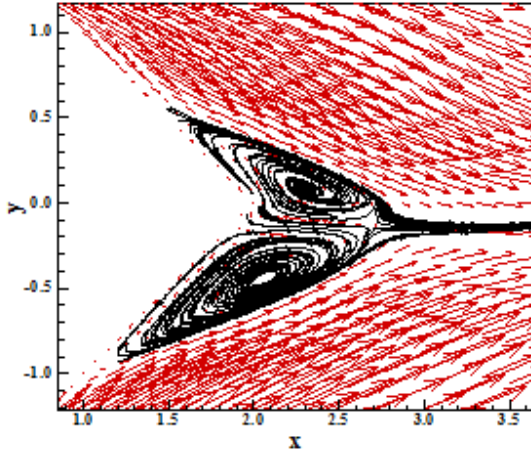


Figure 83: Velocity Field and Streamlines ([2] - SS).

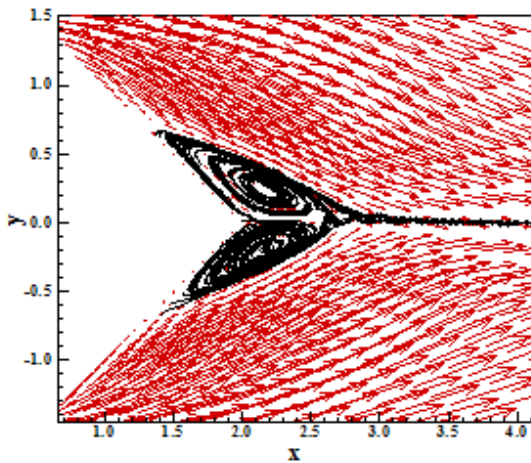


Figure 84: Velocity Field and Streamlines ([2] - AS).

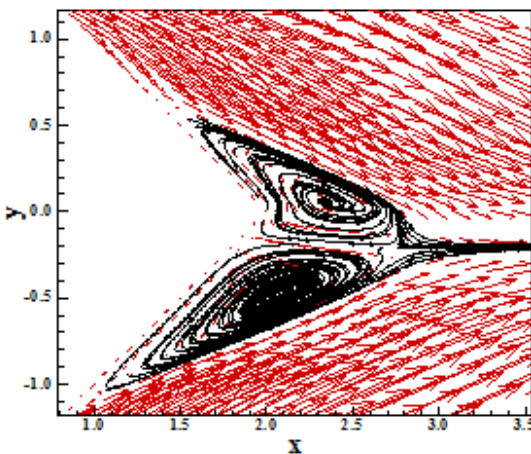


Figure 85: Velocity Field and Streamlines ([4] - SS).

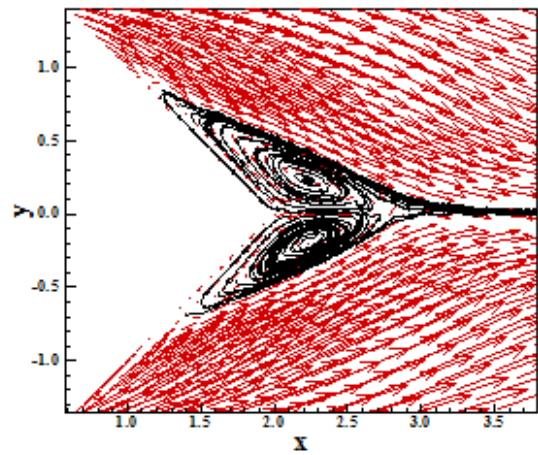


Figure 86: Velocity Field and Streamlines ([4] - AS).

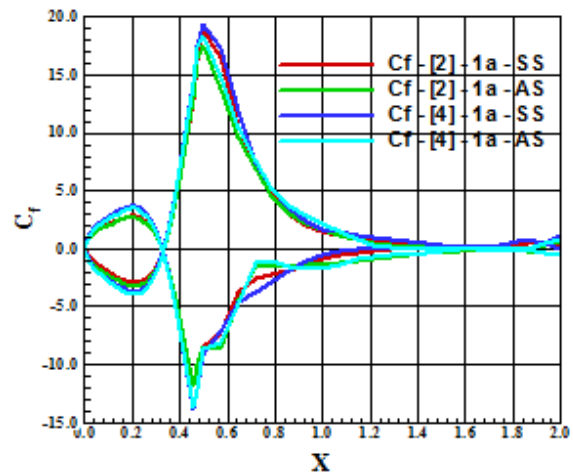


Figure 87: C_f Distribution at Wall.

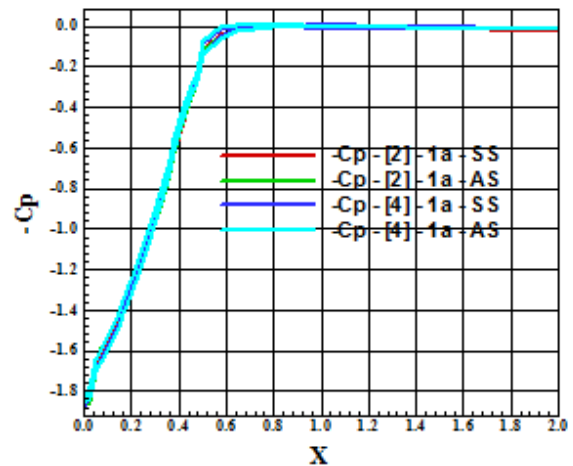


Figure 88: $-C_p$ Distribution at Wall.

Figures 97 to 100 present the vortex field captured by the [2] and [4] numerical schemes in the SS and AS cases. As observed, the solutions obtained in the SS cases are highly non-symmetrical whereas the solutions obtained in the AS cases have

the opposite behavior, presenting good symmetry characteristics.

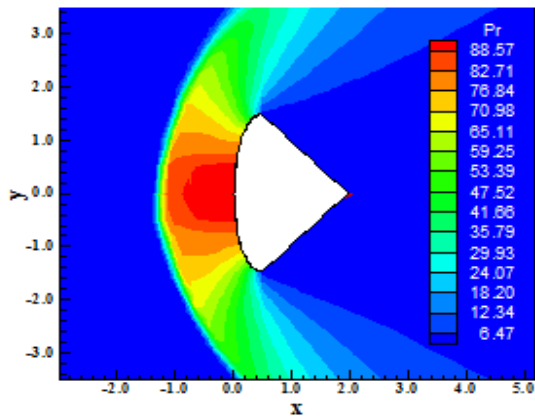


Figure 89: Pressure Field ([2] – SS).

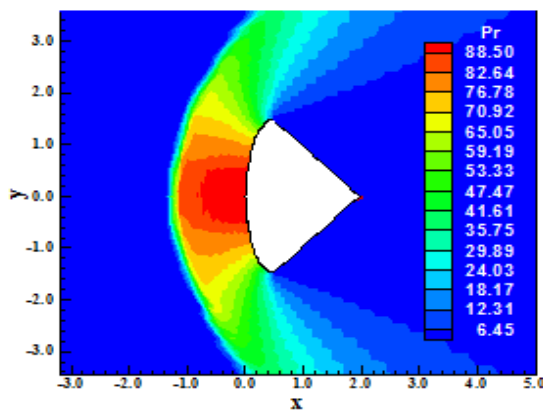


Figure 90: Pressure Field ([2] – AS).

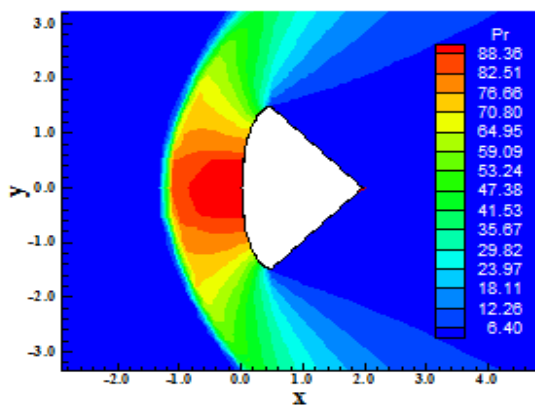


Figure 91: Pressure Field ([4] – SS).

Figure 101 shows the C_f distribution around the re-entry capsule wall. The points of detachment and of reattachment are easily identified. Figure 102 exhibits the $-C_p$ distribution around the re-entry capsule wall. All distributions are similar enough.

Case μ defined according to Sutherland formula. Figures 103 to 106 show the pressure field

obtained by [2] and [4] in the SS and AS cases. As can be observed, good symmetry properties are noted in all solutions. The most severe pressure field is obtained by the [2] algorithm in the SS case. This behavior is observed in all studied cases until now.

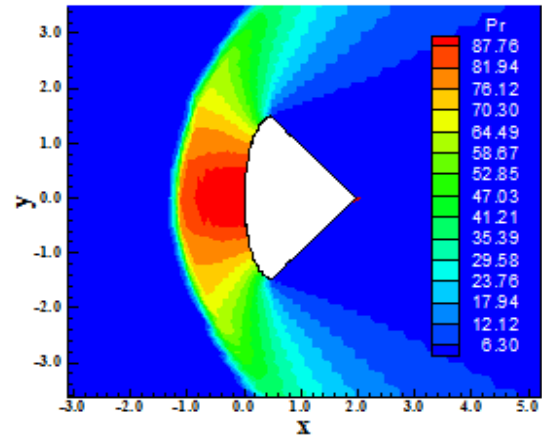


Figure 92: Pressure Field ([4] – AS).

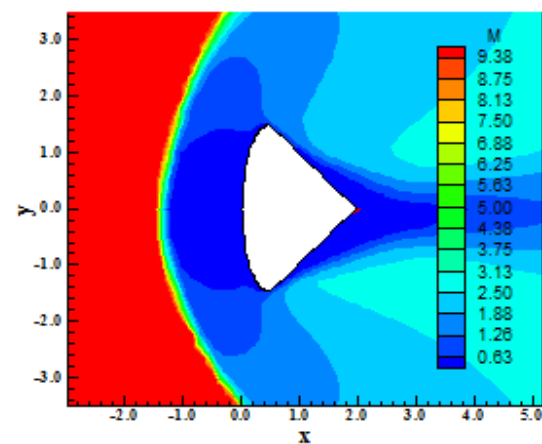


Figure 93: Mach Number Field ([2] – SS).

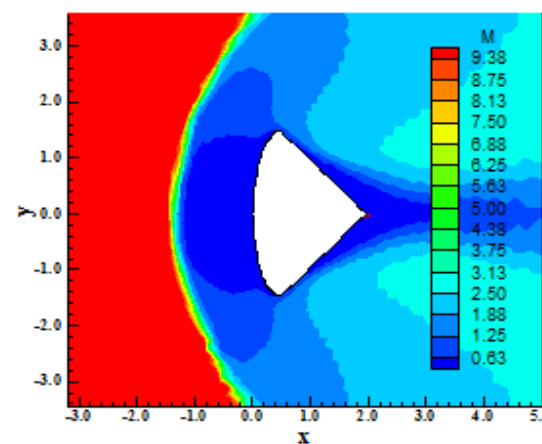


Figure 94: Mach Number Field ([2] – AS).

Figures 107 to 110 exhibit the Mach number field obtained by the [2] and [4] algorithms in the

SS and AS cases. All solutions present good symmetry characteristics. The trailing edge region is the one where the symmetry properties are damaged. Figures 111 to 114 present the velocity field highlighting the pair of vortex which is formed at the trailing edge region.

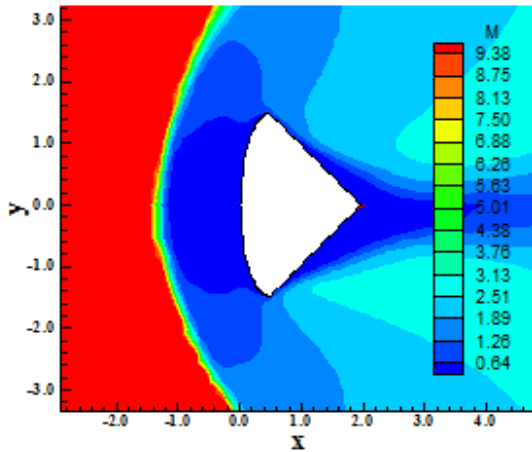


Figure 95: Mach Number Field ([4] - SS).

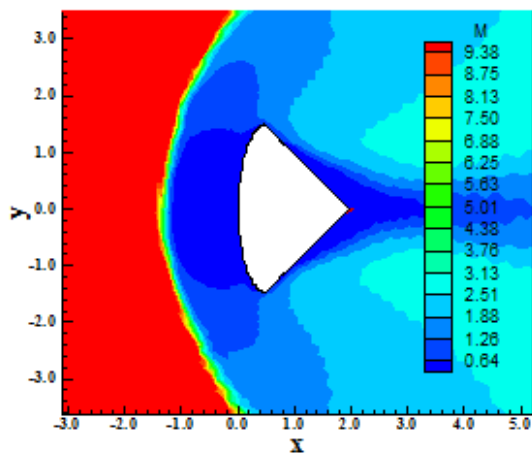


Figure 96: Mach Number Field ([4] - AS).

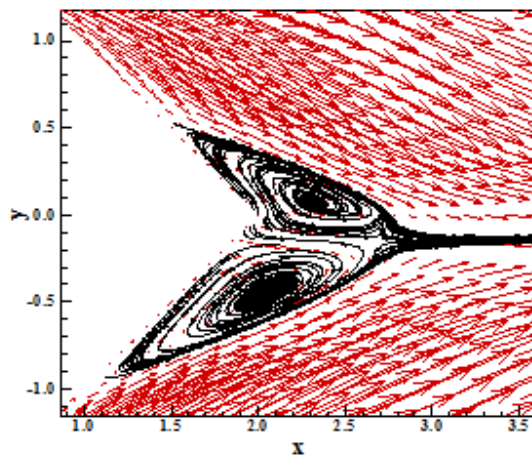


Figure 97: Velocity Field and Streamlines ([2] - SS).

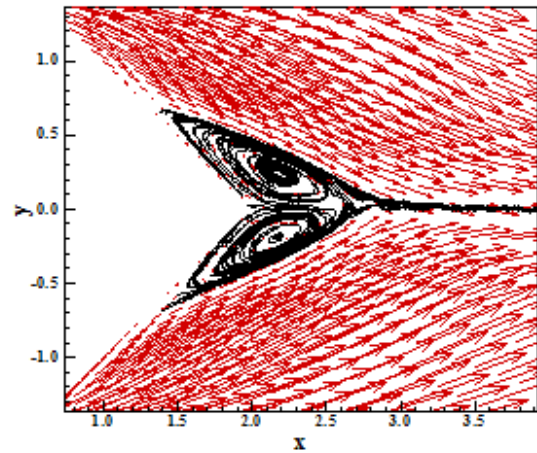


Figure 98: Velocity Field and Streamlines ([2] - AS).

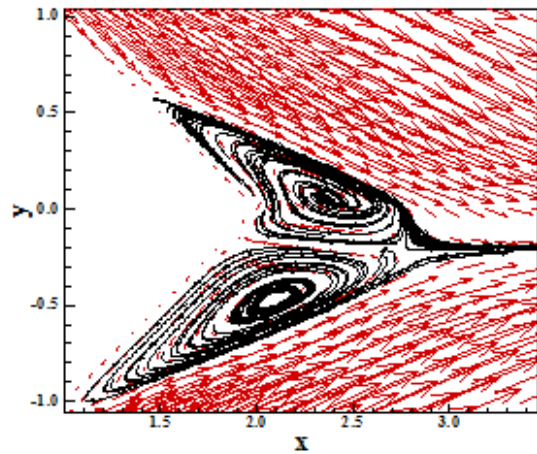


Figure 99: Velocity Field and Streamlines ([4] - SS).

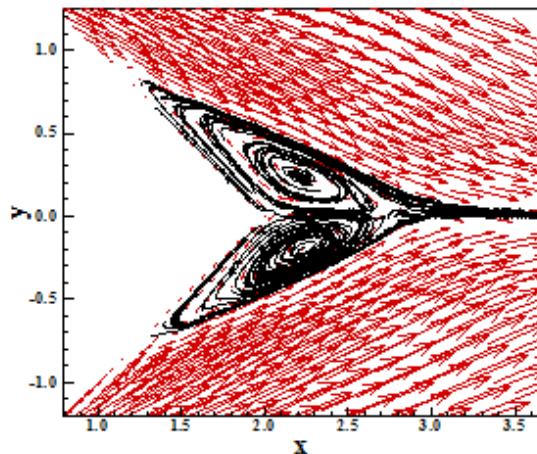


Figure 100: Velocity Field and Streamlines ([4] - AS).

Figure 115 shows the C_f distribution at the reentry capsule wall. Points of detachment and reattachment are approximately 0.32m and 1.60m, respectively. These points of detachment and reattachment define the region of separated flow.

This region initiates at the end of the leading edge region and terminates at the end of the trailing edge one. The C_f distribution should be symmetrical in relation to the x-axis, but due to the unstructured discretization, the non-symmetrical characteristic of the distribution preponderates.

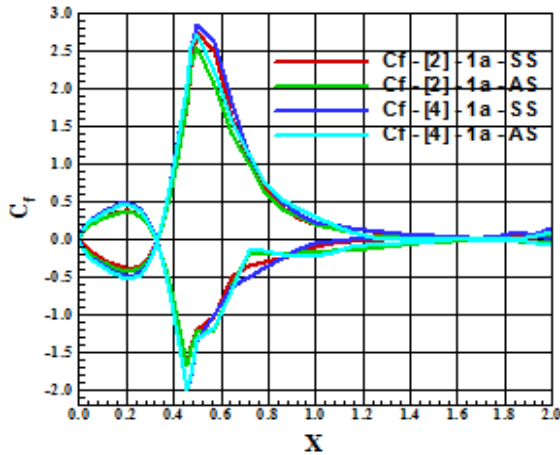


Figure 101: C_f Distribution at Wall.

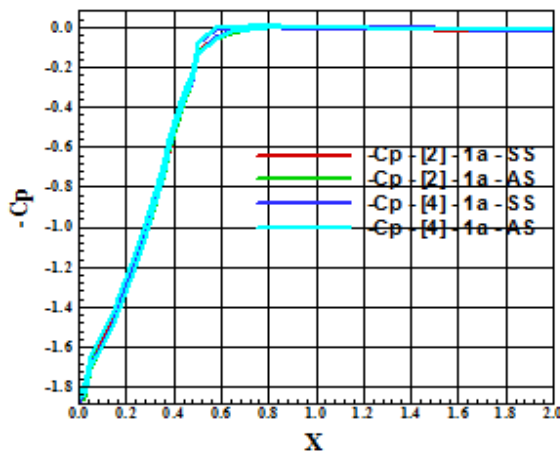


Figure 102: $-C_p$ Distribution at Wall.

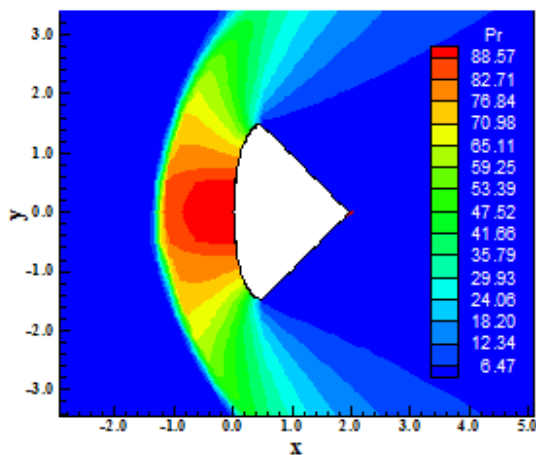


Figure 103: Pressure Field ([2] - SS).

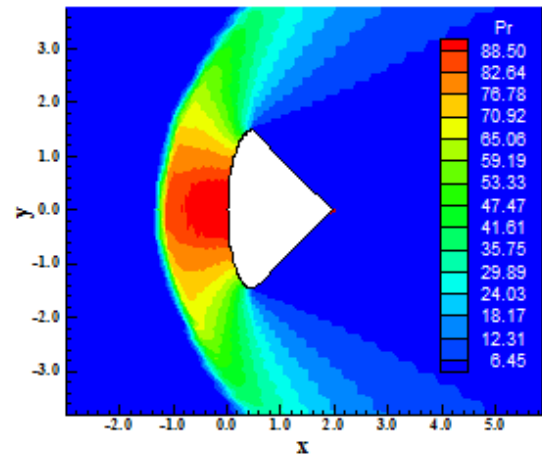


Figure 104: Pressure Field ([2] - AS).

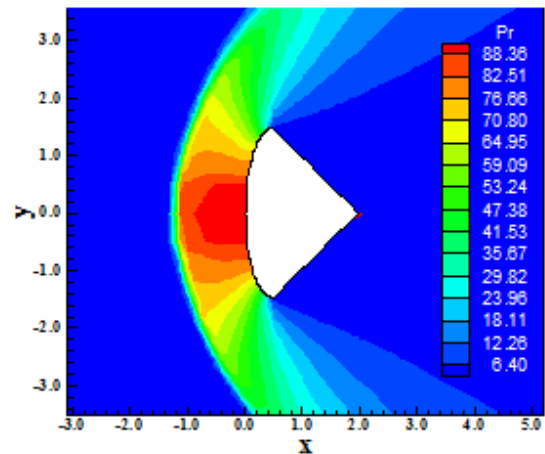


Figure 105: Pressure Field ([4] - SS).

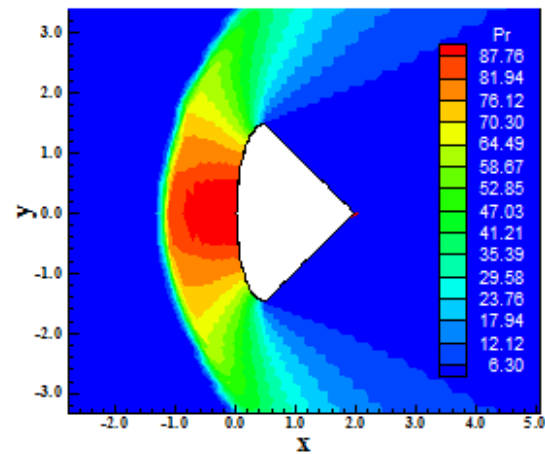


Figure 106: Pressure Field ([4] - AS).

Figure 116 exhibits the $-C_p$ distribution around the re-entry capsule wall. All distributions converge to the same behavior. None of them is better than the other.

Case μ defined according to [11]. Figures 117 to 120 present the pressure field. The most severe pressure field is again obtained by the [2] algorithm and the SS case. Good symmetry properties are observed.

Figures 121 to 124 exhibit the Mach number field obtained by [2] and [4] in the SS and AS cases. The solutions of [4] are more intense than the solutions of [2]. Good symmetry properties are observed.

well captured by [2] and [4]. In the SS case, the pair of vortex presents a non-symmetrical behavior, as expected due to the same triangle orientation adopted for the mesh generation process.

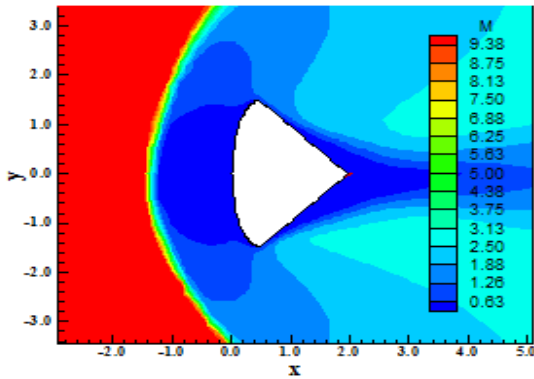


Figure 107: Mach Number Field ([2] – SS).

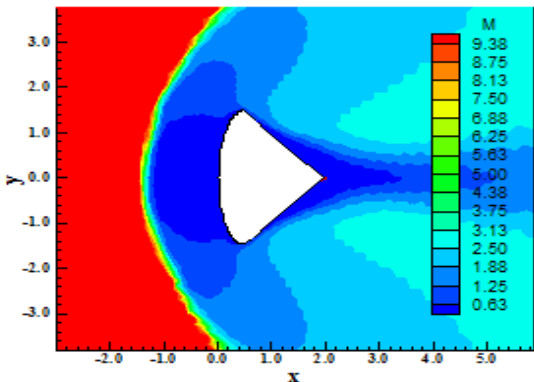


Figure 108: Mach Number Field ([2] – AS).

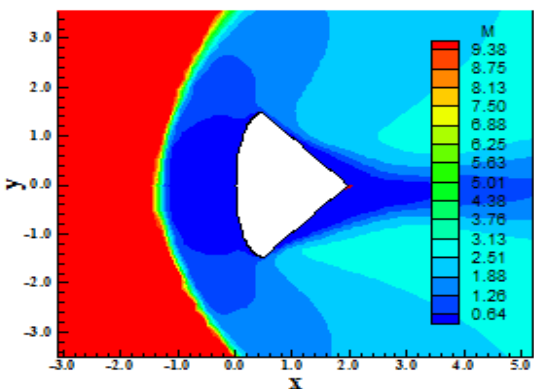


Figure 109: Mach Number Field ([4] – SS).

Figures 125 to 128 show the velocity field highlighting the vortex region. The pair of vortex is

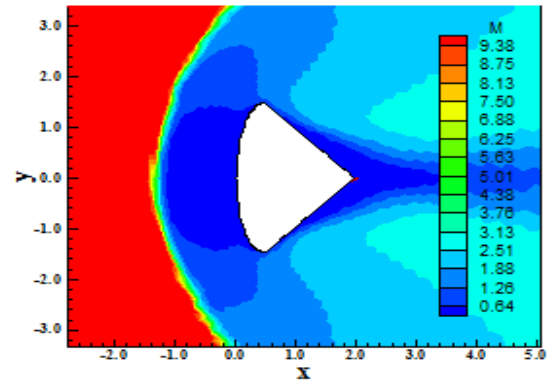


Figure 110: Mach Number Field ([4] – AS).

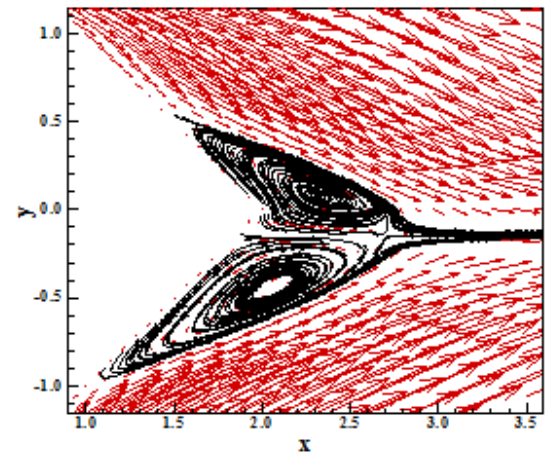


Figure 111: Velocity Field and Streamlines ([2] – SS).

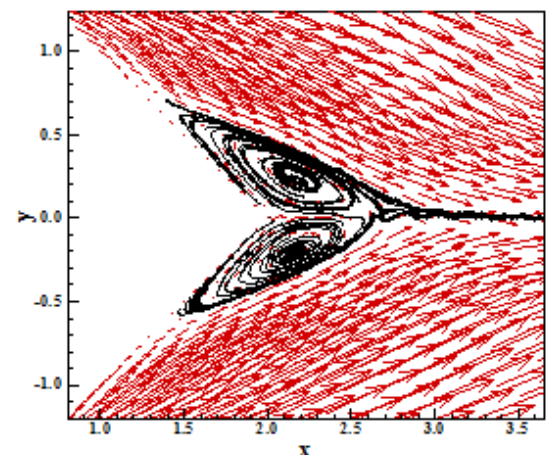


Figure 112: Velocity Field and Streamlines ([2] – AS).

As observed in all studied cases until now, although the “cut out” effect damages lightly the field characteristics, the AS solutions are the best choice to solve unstructured viscous flows in which

symmetry properties are required. In the AS case, the pair of vortex presents a symmetrical behavior, as expected due to the configuration symmetry and the zero value to the attack angle, because the triangle orientation is in clockwise sense in one row and counter-clockwise sense in the following row.

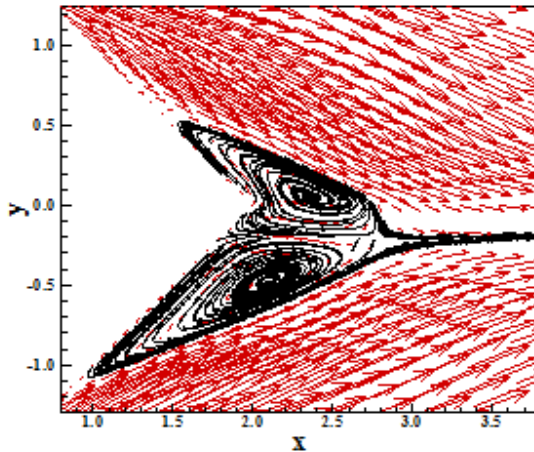


Figure 113: Velocity Field and Streamlines ([4] – SS).

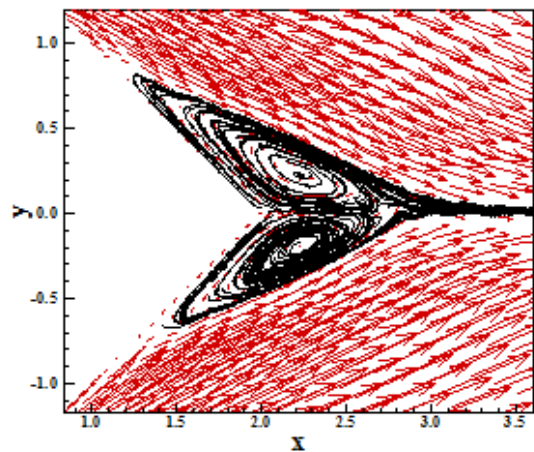


Figure 114: Velocity Field and Streamlines ([4] – AS).

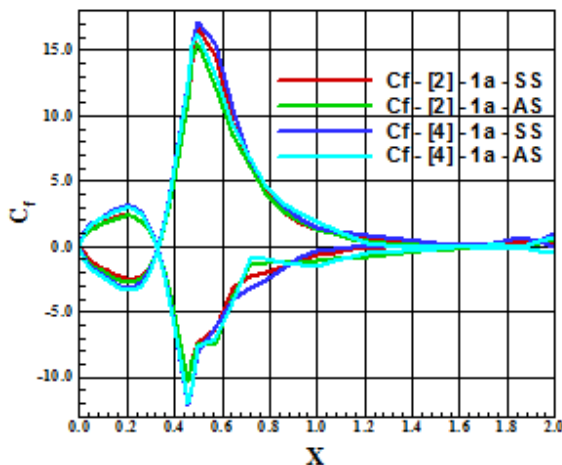


Figure 115: C_f Distribution at Wall.

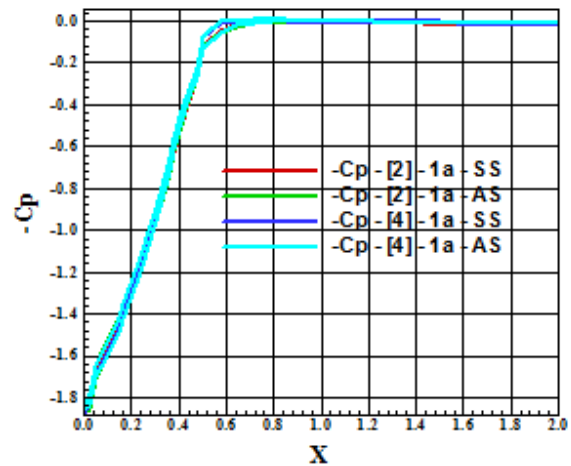


Figure 116: $-C_p$ Distribution at Wall.

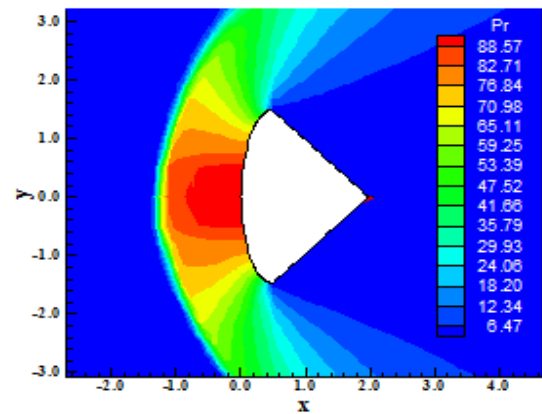


Figure 117: Pressure Field ([2] – SS).

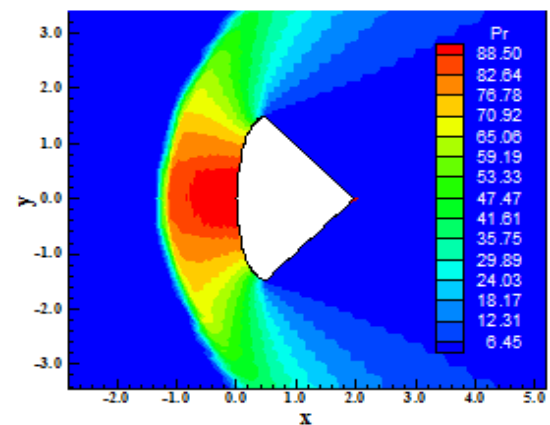


Figure 118: Pressure Field ([2] – AS).

Figure 129 shows the C_f distribution of the friction coefficient. Detachment and reattachment points are easily observed. Figure 130 presents the $-C_p$ distribution at the wall of the re-entry capsule. All solutions exhibit practically the same behavior.

2.2. First Order Turbulent Viscous Solutions – Re-entry Capsule Problem

To this problem a Mach number equal to 10.0 and an attack angle equal to zero was studied. As aforementioned, the mesh employed in the simulations has 10,080 cells and 5,185 nodes.

viscous fluxes and the Sutherland viscosity model was used to calculate the molecular viscosity due to the best behavior observed in the sub-sections above.

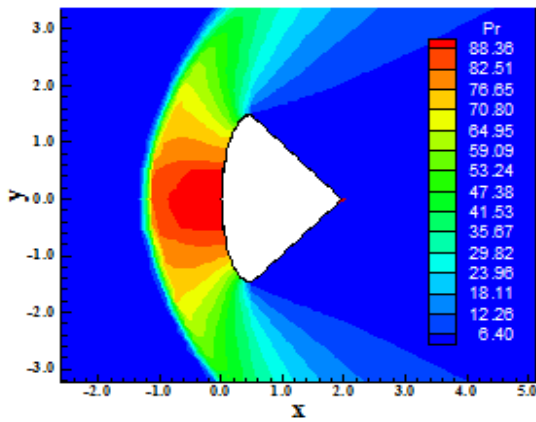


Figure 119: Pressure Field ([4] – SS).

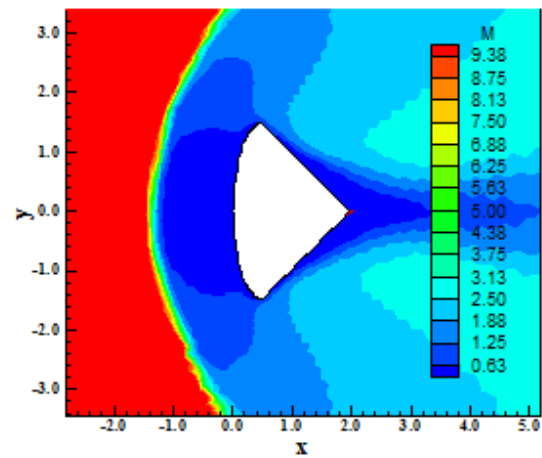


Figure 122: Mach Number Field ([2] – AS).

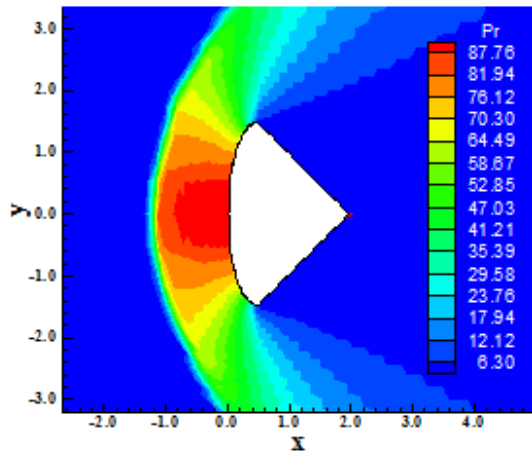


Figure 120: Pressure Field ([4] – AS).

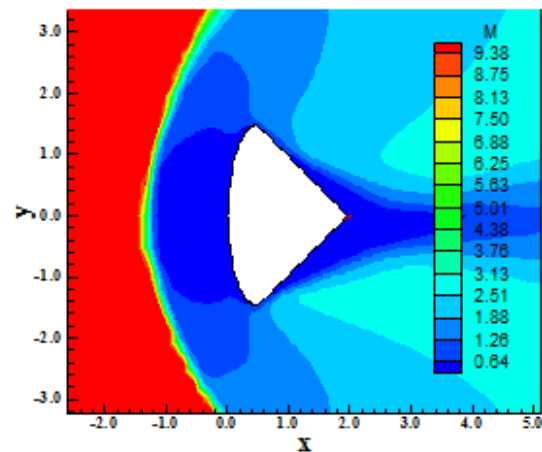


Figure 123: Mach Number Field ([4] – SS).

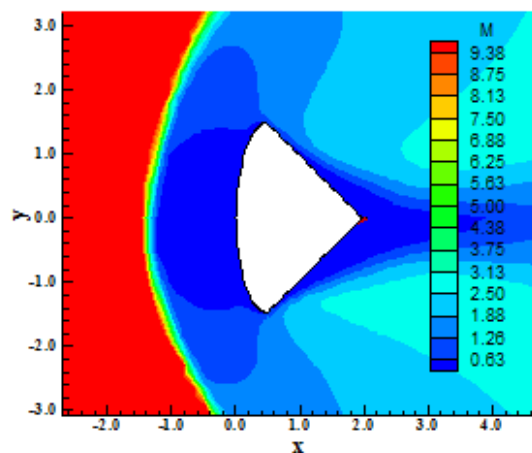


Figure 121: Mach Number Field ([2] – SS).

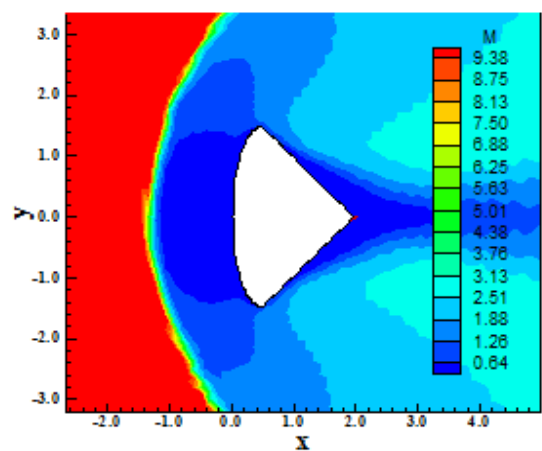


Figure 124: Mach Number Field ([4] – AS).

The characteristic Reynolds number is equal to 2.376×10^6 , which characterizes a turbulent flow. The [6] formulation was employed to calculate the

Figures 131 to 134 present the pressure field obtained by the [2] and [4] algorithms in the SS and

AS cases. The pressure fields have good symmetry properties, with little improvement to the SS solutions. The most severe pressure field is due to [2] in the AS case.

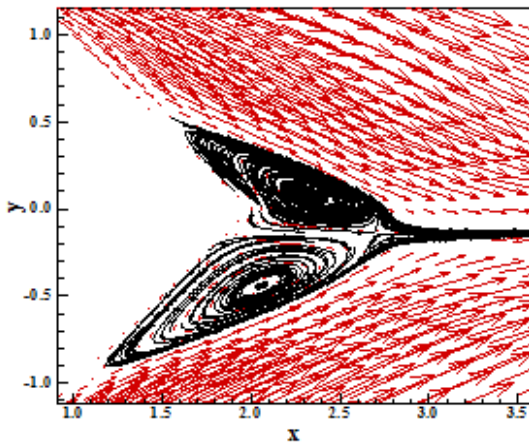


Figure 125: Velocity Field and Streamlines ([2] - SS).

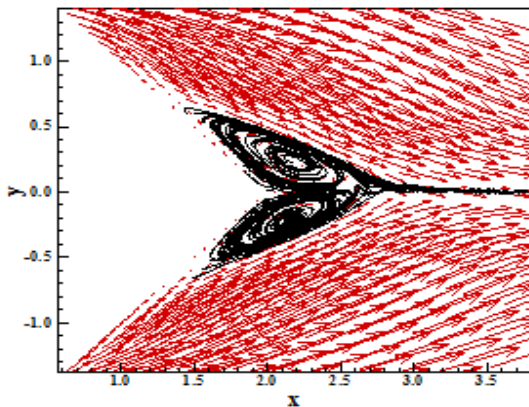


Figure 126: Velocity Field and Streamlines ([2] - AS).

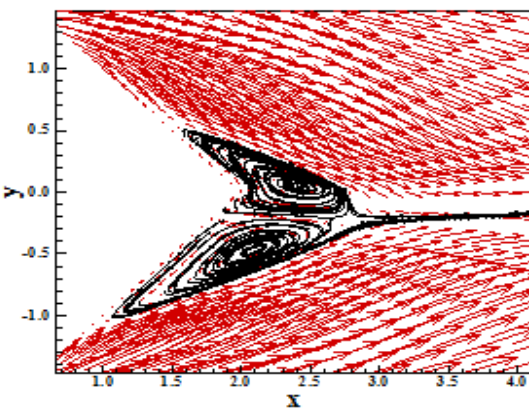


Figure 127: Velocity Field and Streamlines ([4] - SS).

Figures 135 to 138 show the Mach number field obtained by the [2] and [4] schemes in the SS and AS cases. The most intense Mach number field is due to [4] in the SS case. Good symmetry properties are observed in all solutions.

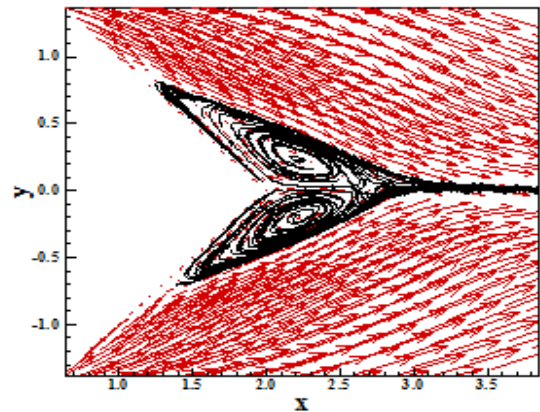


Figure 128: Velocity Field and Streamlines ([4] - AS).

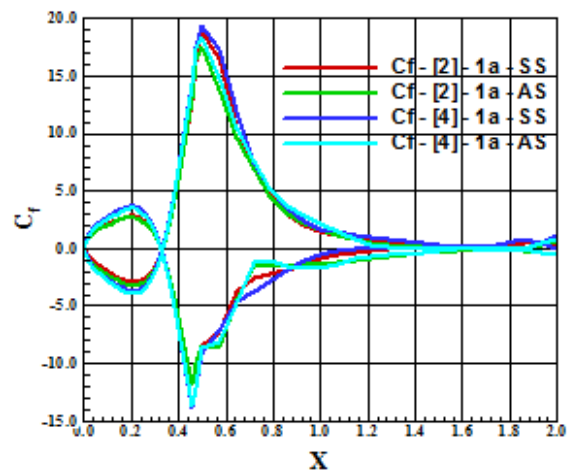


Figure 129: C_f Distribution at Wall.

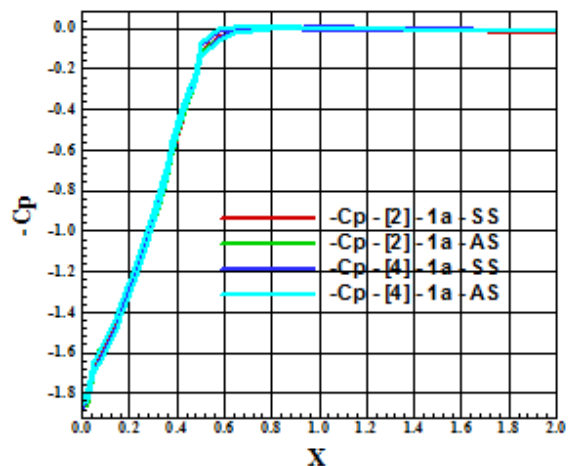


Figure 130: $-C_p$ Distribution at Wall.

Figures 139 to 142 exhibit the velocity vector field highlighting the vortex region at the re-entry capsule trailing edge. The non-symmetry characteristics of the SS case are again observed in the turbulent study. The AS cases yield more symmetrical solutions than their SS contra part. In other words, even as using a turbulence model, this

is not sufficient to repair the non-symmetry of the SS cases.

be close to the laminar results, presenting the values of 0.32m and 1.60m as reasonable ones.

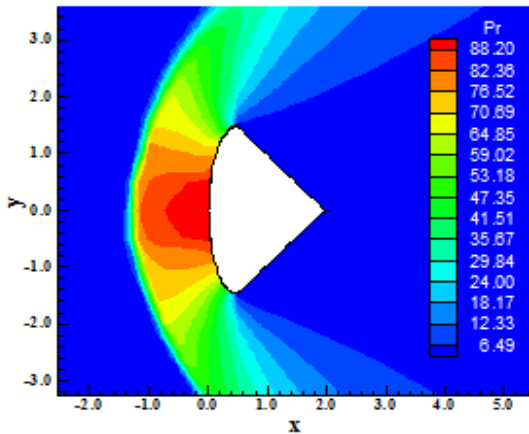


Figure 131: Pressure Field ([2]-SS).

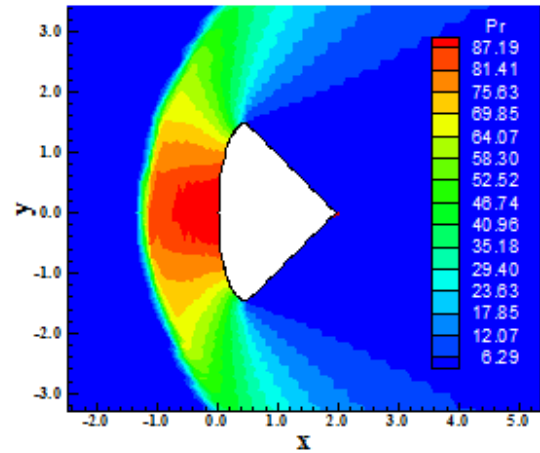


Figure 134: Pressure Field ([4]-AS).

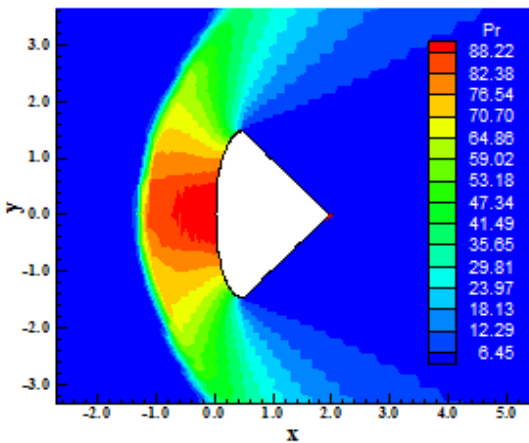


Figure 132: Pressure Field ([2]-AS).

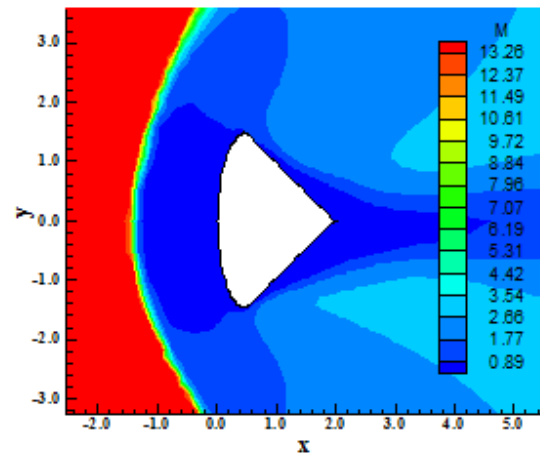


Figure 135: Mach Number Field ([2]-SS).

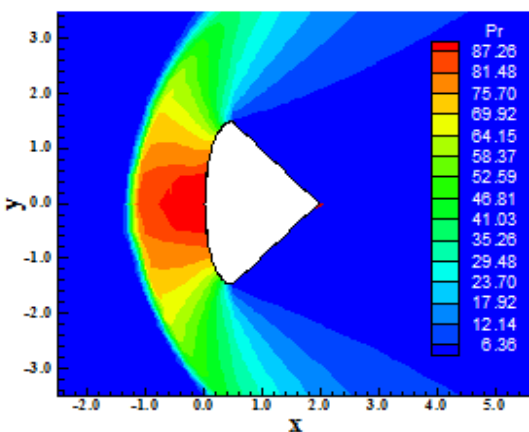


Figure 133: Pressure Field ([4]-SS).

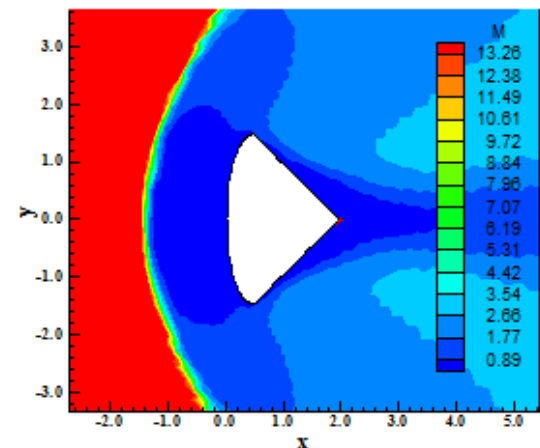


Figure 136: Mach Number Field ([2]-AS).

So, it is possible to conclude that this non-symmetry effect of the SS cases is of geometrical nature and is independent of the flow nature.

Figure 143 exhibits the C_f distribution at wall. The points of detachment and reattachment seem to

Figure 144 shows the kinetic turbulent energy profile at node 74. This result is reasonable, being comparable to the work of [12]. Figure 145 exhibits

the vorticity profile at node 74. The values assumed to the vorticity profile accord to the reference literature.

very similar, with the [4] algorithm in the case AS presenting a fast establishment of the pressure plateau.

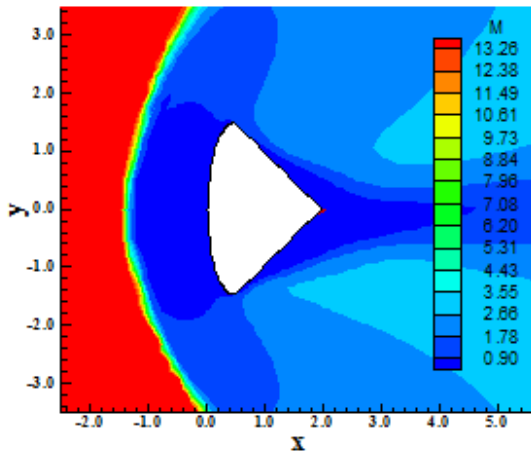


Figure 137: Mach Number Field ([4]-SS).

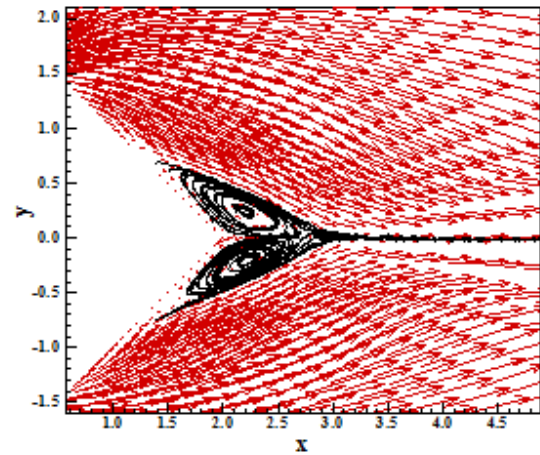


Figure 140: Velocity Field and Streamlines ([2]-AS).

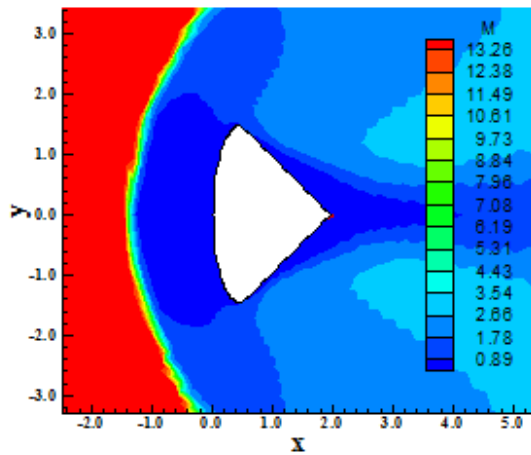


Figure 138: Mach Number Field ([4]-AS).

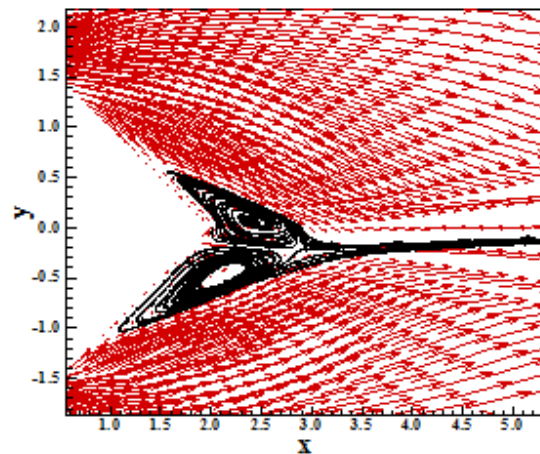


Figure 141: Velocity Field and Streamlines ([4]-SS).

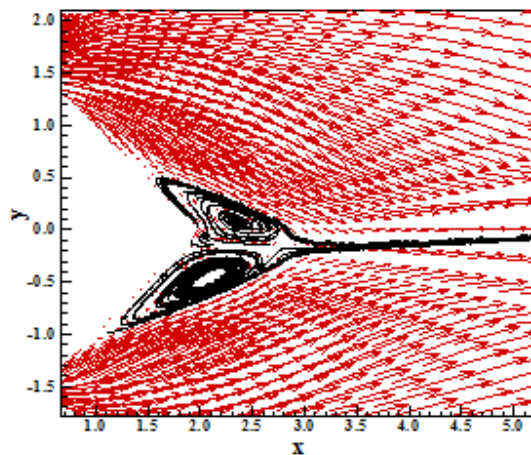


Figure 139: Velocity Field and Streamlines ([2]-SS).

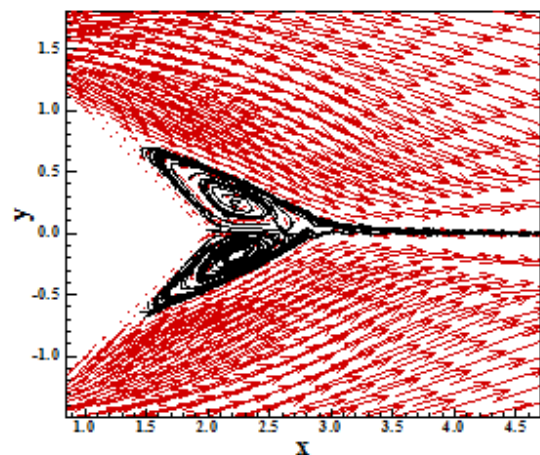


Figure 142: Velocity Field and Streamlines ([4]-AS).

Figure 146 presents the $-C_p$ distribution of [2] and [4] in the SS and AS cases. All distributions are

2.4 Estimation of Lift and Drag Coefficients and of the Stagnation Pressure

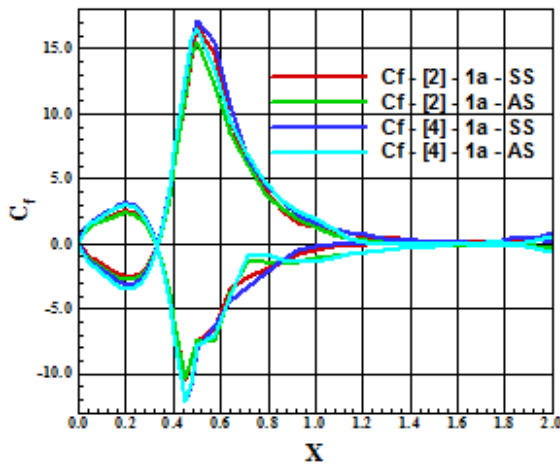


Figure 143: C_f Distribution at Wall.

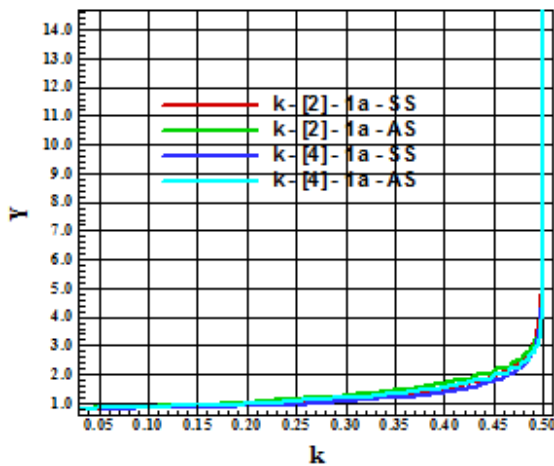


Figure 144: Kinetic Turbulent Energy Profile (node 74).

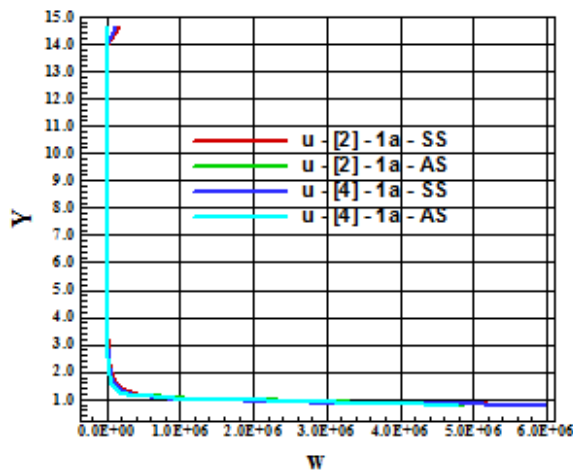


Figure 145: Vorticity Profile (node 74).

The lift and drag aerodynamic coefficients to the re-entry capsule configuration, obtained by the schemes [2] and [4], are presented in Tab. 3. As the geometry is symmetrical and the attack angle of the simulations was considered equal to zero, the

expected value to the aerodynamic coefficient of lift is zero. The [4] scheme, in the SS case, using the [9] turbulence model, presents a c_L closer to the expected value. The major value to the drag coefficient is 2.23261 and is due to [2] in SS cases.

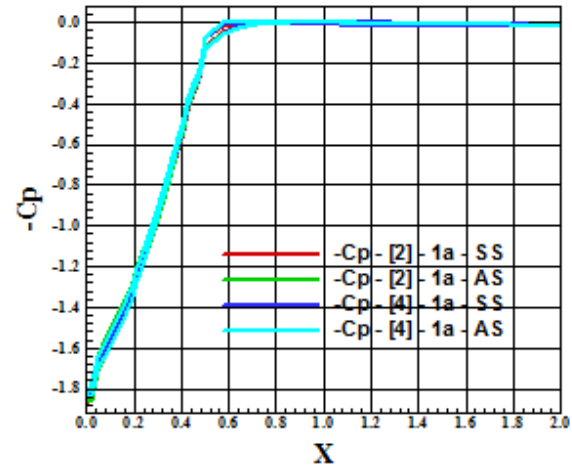


Figure 146: $-C_p$ Distribution at Wall.

One possibility to quantitative analysis of both schemes is the determination of the stagnation pressure ahead of the configuration. [13] presents a table of normal shock wave properties in its B Appendix. This table permits the determination of some shock wave properties as function of the freestream Mach number. In front of the re-entry capsule configuration studied in this work, the shock wave presents a normal shock behavior, which permits the determination of the stagnation pressure, behind the shock wave, from the tables encountered in [13]. So it is possible to determine the ratio pr_0/pr_∞ from [13], where pr_0 is the stagnation pressure in front of the configuration and pr_∞ is the freestream pressure (equals to $1/\gamma$ by the present nondimensionalization).

Hence, to this problem, $M_\infty = 10.0$ corresponds to $pr_0/pr_\infty = 129.2$ and remembering that $pr_\infty = 0.714$, it is possible to conclude that $pr_0 = 92.25$. Table 4 presents the values of the stagnation pressure obtained by each type of flow, each model, each scheme and the respective percentage errors. Values of the percentage error indicate the [2] scheme in the SS cases as the most accurate.

Flow:	Model:	Scheme:	c_L :	c_D :
		[2] - SS	-0.0036	2.2325
	LKS ⁽¹⁾	[2] - AS	-0.0177	2.2324

Laminar	$\mu = \mu_\infty$	[4] – SS	0.0027	2.2194
		[4] – AS	-0.0201	2.2225
	LKS	[2] – SS	-0.0036	2.2326
		[2] – AS	-0.0177	2.2325
	Sutherland	[4] – SS	0.0027	2.2195
		[4] – AS	-0.0201	2.2225
	LKS	[2] – SS	-0.0036	2.2326
		[2] – AS	-0.0177	2.2325
	[11]	[4] – SS	0.0027	2.2195
		[4] – AS	-0.0201	2.2225
Laminar	JK ⁽²⁾ /FPP ⁽³⁾	[2] – SS	-0.0036	2.2325
		[2] – AS	-0.0177	2.2324
	$\mu = \mu_\infty$	[4] – SS	0.0027	2.2194
		[4] – AS	-0.0201	2.2225
	JK/FPP	[2] – SS	-0.0036	2.2326
		[2] – AS	-0.0177	2.2325
	Sutherland	[4] – SS	0.0027	2.2195
		[4] – AS	-0.0201	2.2225
	JK/FPP	[2] – SS	-0.0036	2.2326
		[2] – AS	-0.0177	2.2325
[11]	[4] – SS	0.0027	2.2195	
	[4] – AS	-0.0201	2.2225	
Laminar	JK/JK	[2] – SS	-0.0036	2.2325
		[2] – AS	-0.0177	2.2324
	$\mu = \mu_\infty$	[4] – SS	0.0027	2.2194
		[4] – AS	-0.0201	2.2225
	JK/JK	[2] – SS	-0.0036	2.2326
		[2] – AS	-0.0177	2.2325
	Sutherland	[4] – SS	0.0027	2.2195
		[4] – AS	-0.0201	2.2225

Laminar	JK/JK [11]	[2] – SS	-0.0036	2.2326
		[2] – AS	-0.0177	2.2325
		[4] – SS	0.0027	2.2195
		[4] – AS	-0.0201	2.2225
Turbulent	WR ⁽⁴⁾ Sutherland	[2] – SS	-0.0046	2.2189
		[2] – AS	-0.0202	2.2244
		[4] – SS	-0.0005	2.2130
		[4] – AS	-0.0184	2.2180

⁽¹⁾: LKS = [8]; ⁽²⁾: JK = [7]; ⁽³⁾: FPP = [6]; ⁽⁴⁾: WR = [9].

Table 3: Lift and Drag Aerodynamic Coefficients.

Flow:	Model:	Scheme:	pr ₀ :	Error (%):
Laminar	$\mu = \mu_\infty$	[2] – SS	88.57	3.99
		[2] – AS	88.50	4.07
		[4] – SS	88.36	4.22
		[4] – AS	87.76	4.87
	LKS	[2] – SS	88.57	3.99
		[2] – AS	88.50	4.07
		[4] – SS	88.36	4.22
		[4] – AS	87.76	4.87
	[11]	[2] – SS	88.57	3.99
		[2] – AS	88.50	4.07
		[4] – SS	88.36	4.22
		[4] – AS	87.76	4.87
Laminar	JK ⁽²⁾ /FPP ⁽³⁾	[2] – SS	88.57	3.99
		[2] – AS	88.50	4.07
		[4] – SS	88.36	4.22
		[4] – AS	87.76	4.87
	JK/FPP	[2] – SS	88.57	3.99
		[2] – AS	88.50	4.07
		[4] – SS	88.36	4.22
		[4] – AS	88.36	4.22

		[4] – AS	87.76	4.87	
	JK/FPP [11]	[2] – SS	88.57	3.99	
		[2] – AS	88.50	4.07	
		[4] – SS	88.36	4.22	
		[4] – AS	87.76	4.87	
Laminar	JK/JK $\mu = \mu_\infty$	[2] – SS	88.57	3.99	
		[2] – AS	88.50	4.07	
		[4] – SS	88.36	4.22	
		[4] – AS	87.76	4.87	
	JK/JK Sutherland	[2] – SS	88.57	3.99	
		[2] – AS	88.50	4.07	
		[4] – SS	88.36	4.22	
		[4] – AS	87.76	4.87	
	JK/JK [11]	[2] – SS	88.57	3.99	
		[2] – AS	88.50	4.07	
		[4] – SS	88.36	4.22	
		[4] – AS	87.76	4.87	
Turbulent	WR ⁽⁴⁾ Sutherland	[2] – SS	88.20	4.39	
		[2] – AS	88.22	4.37	
		[4] – SS	87.26	5.41	
			[4] – AS	87.19	5.49

⁽¹⁾: LKS = [8]; ⁽²⁾: JK = [7]; ⁽³⁾: FPP = [6]; (4): WR = [9].

Table 4: Stagnation Pressure and Percentage Error.

2.5 Estimation of the Computational Cost

Table 5 exhibits the computational cost of the numerical schemes studied in this work. They are given in seconds/per cell/per iteration. As can be seen, the cheapest scheme is the [2] algorithm, in the AS case, employing the [8] viscous model, the $\mu = \mu_\infty$ viscosity model, using a CFL number of 0.2 and having a computational cost of 0.0000617sec/per cell/per iteration. The most expensive scheme is the [2] algorithm, in the SS case, employing the [7] viscous model, the Sutherland viscosity model, using a CFL number of 0.2 and having a computational cost of 0.0001036sec/per cell/per iteration.

As the turbulence model employed the [8] (LKS) viscous model to perform the viscous calculation, the Sutherland formula was employed because provides the best cost-benefit relation, being a variable in space and time viscosity model, therefore more accurate, and yielding moderate computational cost. The turbulence model employing the Sutherland formula presented moderate computational costs to the [2] and [4] algorithms in the SS and AS cases.

Scheme:	Case:	Viscous Model:	Interpolation Model:	Viscosity Model:	CFL:	Cost ⁽¹⁾ :
[2]	SS	LKS	-	$\mu = \mu_\infty$	0.2	0.0000618
[2]	SS	LKS	-	Sutherland	0.2	0.0000631
[2]	SS	LKS	-	[11]	0.2	0.0000648
[2]	AS	LKS	-	$\mu = \mu_\infty$	0.2	0.0000617
[2]	AS	LKS	-	Sutherland	0.2	0.0000626
[2]	AS	LKS	-	[11]	0.2	0.0000629
[4]	SS	LKS	-	$\mu = \mu_\infty$	0.4	0.0000640
[4]	SS	LKS	-	Sutherland	0.4	0.0000647
[4]	SS	LKS	-	[11]	0.4	0.0000651
[4]	AS	LKS	-	$\mu = \mu_\infty$	0.4	0.0000637
[4]	AS	LKS	-	Sutherland	0.4	0.0000646
[4]	AS	LKS	-	[11]	0.4	0.0000688
[2]	SS	JK	FPP	$\mu = \mu_\infty$	0.2	0.0000910
[2]	SS	JK	FPP	Sutherland	0.2	0.0000910
[2]	SS	JK	FPP	[11]	0.2	0.0000922
[2]	AS	JK	FPP	$\mu = \mu_\infty$	0.2	0.0000970
[2]	AS	JK	FPP	Sutherland	0.2	0.0000908
[2]	AS	JK	FPP	[11]	0.2	0.0000919
[4]	SS	JK	FPP	$\mu = \mu_\infty$	0.4	0.0000994
[4]	SS	JK	FPP	Sutherland	0.4	0.0001007
[4]	SS	JK	FPP	[11]	0.4	0.0000936
[4]	AS	JK	FPP	$\mu = \mu_\infty$	0.4	0.0000992
[4]	AS	JK	FPP	Sutherland	0.4	0.0001002
[4]	AS	JK	FPP	[11]	0.4	0.0000928
[2]	SS	JK	JK	$\mu = \mu_\infty$	0.2	0.0000946
[2]	SS	JK	JK	Sutherland	0.2	0.0001036
[2]	SS	JK	JK	[11]	0.2	0.0000991

[2]	AS	JK	JK	$\mu = \mu_\infty$	0.2	0.0000906
[2]	AS	JK	JK	Sutherland	0.2	0.0000917
[2]	AS	JK	JK	[11]	0.2	0.0000917
[4]	SS	JK	JK	$\mu = \mu_\infty$	0.4	0.0000927
[4]	SS	JK	JK	Sutherland	0.4	0.0000939
[4]	SS	JK	JK	[11]	0.4	0.0000955
[4]	AS	JK	JK	$\mu = \mu_\infty$	0.4	0.0000929
[4]	AS	JK	JK	Sutherland	0.4	0.0000935
[4]	AS	JK	JK	[11]	0.4	0.0000937
[2]	SS	WR	-	Sutherland	0.2	0.0000872
[2]	AS	WR	-	Sutherland	0.2	0.0000873
[4]	SS	WR	-	Sutherland	0.2	0.0000877
[4]	AS	WR	-	Sutherland	0.1	0.0000876

⁽¹⁾: Given in seconds/per iteration/per cell.

Table 5: Computational Cost of the Numerical Schemes.

3 Conclusions

In this work, numerical simulations involving supersonic and hypersonic flows on an unstructured context were analyzed. The [2] and [4] schemes were implemented on a finite volume formulation, using unstructured spatial discretization. The algorithms were implemented in their first order spatial accuracy to the viscous problem. Two types of linear interpolation, based on the works of [6] and [7], were studied. Two types of viscous calculation to the laminar case were compared. They were programmed considering the works of [7] and [8]. To the turbulent simulations, the [9] model was employed. The ramp problem to the supersonic inviscid case and the re-entry capsule problem to the hypersonic viscous case were considered. The results have demonstrated that the [2] algorithm yielded the best results in terms of the prediction of the wall pressure distribution and shock angle in the inviscid simulations and the best value of the stagnation pressure at the configuration nose in the viscous simulations.

4 Acknowledgments

The present author acknowledges the CNPq by the financial support conceded under the form of a DTI (Industrial Technological Development) scholarship no. 384681/2011-5. He also acknowledges the infra-

structure of the ITA that allowed the realization of this work.

References:

- [1] P. Kutler, Computation of Three-Dimensional, Inviscid Supersonic Flows, *Lecture Notes in Physics*, Vol. 41, 1975, pp. 287-374.
- [2] B. Van Leer, Flux-Vector Splitting for the Euler Equations, Proceedings of the 8th International Conference on Numerical Methods in Fluid Dynamics, E. Krause, Editor, *Lecture Notes in Physics*, Vol. 170, 1982, pp. 507-512, Springer-Verlag, Berlin.
- [3] M. Liou, and C. J. Steffen Jr., A New Flux Splitting Scheme, *Journal of Computational Physics*, Vol. 107, 1993, pp. 23-39.
- [4] R. Radespiel, and N. Kroll, Accurate Flux Vector Splitting for Shocks and Shear Layers, *Journal of Computational Physics*, Vol. 121, 1995, pp. 66-78.
- [5] E. S. G. Maciel, Supersonic and Hypersonic Flows on 2D Unstructured Context: Part I, WSEAS on Fluid Dynamics, *WSEAS 53-669*, 2011.
- [6] N. T. Frink, P. Parikh, and S. Pirzadeh, Aerodynamic Analysis of Complex Configurations Using Unstructured Grids, *AIAA 91-3292-CP*, 1991.
- [7] F. Jacon, and D. Knight, A Navier-Stokes Algorithm for Turbulent Flows Using an Unstructured Grid and Flux Difference Splitting, *AIAA Paper 94-2292*, 1994.
- [8] L. N. Long, M. M. S. Khan, and H. T. Sharp, Massively Parallel Three-Dimensional Euler / Navier-Stokes Method, *AIAA Journal*, Vol. 29, 1991, No. 5, pp. 657-666.
- [9] D. C. Wilcox, and M. W. Rubesin, Progress in Turbulence Modeling for Complex Flow Fields Including the Effects of Compressibility, *NASA TP-1517*, 1980.
- [10] R. W. Fox, and A. T. McDonald, *Introdução à Mecânica dos Fluidos*, Ed. Guanabara Koogan, Rio de Janeiro, RJ, Brazil, 632 p, 1988.
- [11] D. J. Mavriplis, and A. Jameson, Multigrid Solution of the Navier-Stokes Equations on Triangular Meshes, *AIAA Journal*, Vol. 28, 1990, No. 8, pp. 1415-1425.
- [12] E. S. G. Maciel, and N. G. C. R. Fico Jr., Comparação Entre Modelos de Turbulência de Duas Equações Aplicados a um Problema Aeroespacial, *Anales del Primer Congreso Argentino de Ingeniería Mecánica (I CAIM)*, Bahía Blanca, Argentina, 2008.
- [13] J. D. Anderson Jr., *Fundamentals of Aerodynamics*, McGraw-Hill, Inc., EUA, 563p, 1984.